

# Regulation of adenylyl cyclase 5 in striatal neurons confers the ability to detect coincident neuromodulatory signals

Neil J. Bruce<sup>1,\*</sup>  
Daniele Narzi<sup>2,\*</sup>  
Daniel Trpevski<sup>3,\*</sup>  
Siri Camee van Keulen<sup>2,4,\*</sup>  
Anu G. Nair<sup>5</sup>  
Ursula Röthlisberger<sup>2,+</sup>  
Rebecca C. Wade<sup>1,6,7,+</sup>  
Paolo Carloni<sup>8,9,+</sup>  
Jeanette Hellgren Kotaleski<sup>3,10,+</sup>

\*: Joint first authors

+: Corresponding Authors

## Affiliations:

1. Molecular and Cellular Modeling Group, Heidelberg Institute for Theoretical Studies (HITS), Schloss-Wolfsbrunnengasse 35, 69118 Heidelberg, Germany.

2. Institut des Sciences et Ingénierie Chimiques, École Polytechnique Fédérale de Lausanne (EPFL), CH-1015 Lausanne, Switzerland

3. Science for Life Laboratory, School of Computer Science and Communication, KTH Royal Institute of Technology, 10044, Stockholm, Sweden.

4. Department of Computer Science, Stanford University, Stanford, California 94305, USA

5. Institute of Molecular Life Sciences, University of Zurich, Winterthurerstrasse 190, 8057 Zurich, Switzerland

6. Center for Molecular Biology (ZMBH), DKFZ-ZMBH Alliance, Heidelberg University, Im Neuenheimer Feld 282, 69120 Heidelberg, Germany

7. Interdisciplinary Center for Scientific Computing (IWR), Heidelberg University, Im Neuenheimer Feld 368, 69120 Heidelberg, Germany

8. Department of Physics and Department of Neurobiology, RWTH Aachen University, 52078 Aachen, Germany

9. Institute for Neuroscience and Medicine (INM)-11, Forschungszentrum Jülich, 52428 Jülich, Germany, Institute of Neuroscience and Medicine (INM-9) and Institute for Advanced

Simulation (IAS-5), Forschungszentrum Jülich, Wilhelm-Johnen-Strasse,  
52425 Jülich, Germany  
10. Department of Neuroscience, Karolinska Institutet, 17177, Solna,  
Sweden.

## Abstract

Long-term potentiation and depression of synaptic activity in response to stimuli is a key factor in reinforcement learning. Strengthening of the corticostriatal synapses depends on the second messenger cAMP, whose synthesis is catalysed by the enzyme adenylyl cyclase 5 (AC5), which is itself regulated by the stimulatory  $G\alpha_{\text{olf}}$  and inhibitory  $G\alpha_i$  proteins. AC isoforms have been suggested to act as coincidence detectors, promoting cellular responses only when convergent regulatory signals occur close in time. However, the mechanism for this is currently unclear, and seems to lie in their diverse regulation patterns. Despite attempts to isolate the ternary complex, it is not known if  $G\alpha_{\text{olf}}$  and  $G\alpha_i$  can bind to AC5 simultaneously, nor what activity the complex would have. Using protein structure-based molecular dynamics simulations, we show that this complex is stable and inactive. These simulations, along with Brownian dynamics simulations to estimate protein association rates constants, constrain a kinetic model that shows that the presence of this ternary inactive complex is crucial for AC5's ability to detect coincident signals, producing a synergistic increase in cAMP. These results reveal some of the prerequisites for corticostriatal synaptic plasticity, and explain recent experimental data on cAMP concentrations following receptor activation. Moreover, they provide insights into the regulatory mechanisms that control signal processing by different AC isoforms.

## Author summary

Adenylyl cyclases (ACs) are enzymes that can translate extracellular signals into the intracellular molecule cAMP, which is thus a 2<sup>nd</sup> messenger of extracellular events. The brain expresses nine membrane-bound AC variants, and AC5 is the dominant form in the striatum. The striatum is the input stage of the basal ganglia, a brain structure involved in reward learning, i.e. the learning of behaviors that lead to rewarding stimuli (such as food, water, sugar, etc). During reward learning, cAMP production is crucial for strengthening the synapses from cortical neurons onto the striatal principal neurons, and its formation is dependent on several neuromodulatory systems such as dopamine and acetylcholine. It is, however, not understood how AC5 is activated by transient (subsecond) changes in the neuromodulatory signals. Here we combine several computational tools, from molecular dynamics and Brownian dynamics simulations to bioinformatics approaches, to inform and constrain a kinetic model of the AC5-dependent signaling system. We use this model to show how the specific molecular properties of AC5 can detect particular combinations of co-occurring transient changes in the neuromodulatory signals which thus result in a supralinear/synergistic cAMP production. Our results also provide insights into the computational capabilities of the different AC isoforms.

## Introduction

Information processing in the brain occurs within circuits of neurons that are interconnected via synapses. The modification of these neuronal circuits, in response to an organism's experiences and interactions with the environment, is crucial for memory and learning, allowing the organism's behaviour to adapt to changing conditions in its environment. One way that neuronal circuits are modified is through

the process of synaptic plasticity, in which the strengths of certain synapses are either enhanced or depressed over time in response to neural activity. Insights into when plasticity happens can provide an understanding of the basic functioning of the nervous system, and its ability to learn. A very informative way to gain such insights is through analyzing the molecular circuitry of the synapses - i.e. the networks of biochemical reactions that underlie synaptic modifications. These differ across synapses, and our focus in this study is on the corticostriatal synapse, which is the interface between the cortex and the basal ganglia, a forebrain structure involved in selection of behaviour and reward learning (Glatt & Snyder, 1993; Mons & Cooper, 1994).

All cells process information from their external and internal environment through signal transduction networks - molecular circuits evolved for producing suitable responses to different stimuli. In neurons, synaptic signal transduction networks determine whether a synapse will be potentiated or depressed. In some cases, even single molecules are able to realize computational abilities within these networks. These molecules are often enzymes, whose activity is allosterically regulated by the binding of other signaling molecules (Changeux & Edelstein, 2005). One such case is the family of mammalian adenylyl cyclase enzymes (ACs). These catalyze the conversion of adenosine triphosphate (ATP) to cyclic adenosine monophosphate (cAMP) - one of the main cellular second messenger signaling molecules.

Mammalian ACs express ten different isoforms (Linder, 2006; Linder & Schultz, 2003; Sadana & Dessauer, 2009). Of these, nine are membrane bound, and one is soluble. Their catalytic reaction may be regulated by a variety of interactors, most importantly G protein subunits (Sadana & Dessauer, 2009). These are released in response to extracellular agonists binding to G protein-coupled receptors (GPCRs), the largest superfamily of mammalian transmembrane receptors. In this way, ACs may function not only as signal transducers but also as *signal integrators*: they perform decision functions that determine the time at which and how much cAMP is produced. One such decision function, attributed to many ACs, is detection of co-occurring signaling events (denoted as *coincidence detection* here), resulting in significantly increased production of cAMP only when more than one signaling event occurs almost simultaneously (Anholt, 1994; Bourne & Nicoll, 1993; Delmeire et al., 2003; Impey et al, 1994; Lustig et al, 1993; McVey et al, 1999; Mons, Guillou, & Jaffard, 1999; Nair et al, 2019; Nair et al, 2015).



All nine membrane-bound AC isoforms are expressed in the brain, possibly because this organ is specialized in signal processing. Specific ACs are particularly abundant in specific brain regions, and AC5 is highly expressed in the striatum, the input nucleus of the basal ganglia. It is involved in signal transduction networks that are crucial for synaptic plasticity in the two types of medium spiny neurons (MSNs) of this brain region, which are the direct pathway MSNs that express D<sub>1</sub>-type dopamine receptors (D<sub>1</sub> MSNs), and the indirect pathway MSNs expressing D<sub>2</sub>-type dopamine receptors (D<sub>2</sub> MSNs).

The same regulatory mechanism exists in both MSN types: AC5 is activated by the stimulatory G $\alpha_{\text{olf}}$  protein subunit, and inhibited by the inhibitory G $\alpha_{\text{i}}$  protein subunit. Clearly, the regulation of AC5 is a crucial determinant of the levels of cAMP. This mechanism responds to different extracellular agonists (acting as neuromodulatory signals) associated with the expression of different G protein-coupled receptors (GPCRs) (Fig. 1A) (Onali and Olanas, 2002; Jeon et al. 2010; Ferre et al. 2008). In D<sub>1</sub> MSNs, the binding of dopamine to the D<sub>1</sub> GPCR results in the release of G $\alpha_{\text{olf}}$ , while binding of acetylcholine to the M<sub>4</sub> GPCR causes the release of G $\alpha_{\text{i}}$ . Conversely, in D<sub>2</sub> MSNs, binding of dopamine results in the release of G $\alpha_{\text{i}}$ , and G $\alpha_{\text{olf}}$  is released upon binding of adenosine to the A<sub>2a</sub> GPCR.

Knowing how AC5 processes the neuromodulatory signals would reveal the conditions under which plasticity and learning in the basal ganglia are triggered. In particular, knowing whether AC5 is a coincidence detector will help us understand if and why changes in more than one of the neuromodulatory signals it receives are necessary to trigger synaptic plasticity. This is what we have set out to determine in this study. We use the neuromodulation of D<sub>1</sub> MSNs as the example here (see Nair et al, 2015).

At a basal state in the D<sub>1</sub> MSNs, AC5 is inhibited by G $\alpha_{\text{i}}$  due to a tonic level of acetylcholine produced by the tonic activity of the striatal cholinergic interneurons (Nair et al, 2019). Previous modeling studies of this signal transduction network predicted that AC5 responds most strongly to a simultaneous increase in dopamine (Da  $\uparrow$ ) and a pause in acetylcholine levels (ACh  $\downarrow$ ), i.e. both stimulation by increased G $\alpha_{\text{olf}}$  and disinhibition by decreased G $\alpha_{\text{i}}$  are necessary for the enzyme to produce significant amounts of cAMP (Nair et al, 2015). The response to the two neuromodulatory signals was nonlinear and synergistic. This suggests that AC5 might function as a coincidence detector, since the network responds with significant amounts of cAMP only when the two

incoming signals  $Da \uparrow$  and  $ACh \downarrow$  coincide in time and in the spatial vicinity of the receptors. In order to perform strong coincidence detection, the network should be able to make a clear distinction between the situation of a simultaneous dopamine peak and acetylcholine dip ( $Da \uparrow + ACh \downarrow$ ) and that of a single signal, i.e.  $Da \uparrow$  or  $ACh \downarrow$  alone. This distinction is realized by producing different amounts of cAMP, i.e. by differences in the enzyme's catalytic rate.

During the course of our previous kinetic modelling study (Nair et al, 2015), and follow-up experimental studies on the function of the AC5 signal transduction network (Nair et al, 2019; Yapo et al., 2017), it became clear that the presence or absence of a ternary  $G\alpha_{\text{off}} \cdot AC5 \cdot G\alpha_i$  complex during AC5 regulation, and the level of catalytic activity of such a complex, could significantly affect AC5's ability to act as a coincidence detector.

While the existence of the binary  $AC5 \cdot G\alpha_i$  and  $AC5 \cdot G\alpha_{\text{off}}$  complexes, and their catalytic activities, has been confirmed experimentally, a  $G\alpha_{\text{off}} \cdot AC5 \cdot G\alpha_i$  ternary complex has not been identified so far (Tesmer et al, 1997; Dessauer et al, 1998; Tesmer et al, 1999). However, it has been suggested to exist during AC5 regulation, but it is not known whether it would be catalytically active or inactive (Fig. 1B) (Dessauer et al, 1998; Chen-Goodspeed, Lukan, & Dessauer, 2005). So far, we know from molecular dynamics (MD) simulations of the binary complexes that binding of one  $G\alpha$  subunit can produce allosteric effects at the binding site for the other (Van Keulen and Röthlisberger, 2017b; Frezza, Martin, & Lavery, 2018), raising the speculation that allosteric effects influence ternary complex formation.

Resolving the details of AC5 regulation can help to understand whether AC5 acts as a coincidence detector, and hence, whether two neuromodulatory signals are necessary for plasticity and learning in the basal ganglia. Here, we take a multiscale modeling approach to address the following question: can the  $G\alpha_{\text{off}} \cdot AC5 \cdot G\alpha_i$  ternary complex form in the AC5 signal transduction network? If it does, is it able to catalyse ATP conversion, and does its presence affect the ability of the enzyme to perform coincidence detection? We combine MD simulations, to study the complexation of AC5 with its  $G\alpha$  partners, with Brownian dynamics (BD) simulations to estimate the forward (association) rate constants of binding between AC5 and the  $G\alpha$  subunits. Snapshots from the MD simulations are used as starting points for BD simulations. We then incorporate the results from these simulations into a kinetic model of the AC5 signal transduction network and quantify the ability of the enzyme to detect coincident

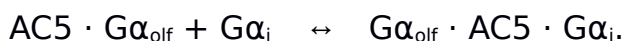
extracellular signaling events. Molecular simulation approaches that bridge multiple spatial and temporal scales are well established (Hollingsworth and Dror, 2018), and here we span the spatial scales by bridging from intra- and inter-molecular dynamics up to the function of a biochemical reaction network (Stein et al., 2007; Boras et al., 2015; Kitano, 2002). Multiscale simulation is particularly informative for this system since experimental efforts in studying the ternary complex have not yielded results.

Our MD simulations show that a ternary complex could be present during AC5 regulation, being stable on the  $\mu\text{s}$  timescale, but it appears to be catalytically inactive. The kinetic model, constructed using results from the MD and BD simulations performed here, reveals that: (i) the suggested interaction scheme between the regulatory  $G\alpha_{\text{olf}}$  subunits and AC5 strengthens coincidence detection when compared to alternative schemes; (ii) the predicted values of the forward rate constants are favourable for coincidence detection. This suggests that AC5 is indeed a powerful coincidence detector and, as a result of the inactive ternary complex, a rise in dopamine alone does not have an effect on synaptic plasticity; it needs to be accompanied by a pause in the level of acetylcholine. These insights are also discussed with regard to other AC isoforms.

## Results

### **Molecular dynamics simulations indicate that the apo $G\alpha_{\text{olf}} \cdot AC5 \cdot G\alpha_i$ ternary complex is stable on microsecond timescales**

The existence of a ternary complex,  $G\alpha_{\text{olf}} \cdot AC5 \cdot G\alpha_i$ , during AC5 regulation has been unclear. So far it has not been possible to detect the complex in experiments, possibly due to its unstable nature (Dessauer et al, 1998). However, as  $G\alpha_{\text{olf}}$  and  $G\alpha_i$  interact with AC5 on different sites on its catalytic domains, the ternary complex could be formed via two reactions:



Previous MD simulation results suggested that upon binding of  $G\alpha_i$  to AC5, the  $G\alpha_{\text{olf}}$  binding groove adopts a conformation that hinders  $G\alpha_{\text{olf}}$  from binding (Van Keulen & Röthlisberger 2017b), making the first reaction less favourable; however, a stable ternary complex might still

be formed via the second route. All-atom MD simulations were employed to investigate the stability of a putative *apo* ternary complex,  $G\alpha_{\text{olf}} \cdot AC5 \cdot G\alpha_i$ , in the absence of ATP, on the  $\mu\text{s}$  time scale. We mention here that  $G\alpha_{\text{olf}}$  has no post-translational modifications to its protein sequence. In contrast,  $G\alpha_i$  is considered in its myristoylated form since a non-myristoylated  $G\alpha_i$  subunit is known to be unable to form an  $AC5 \cdot G\alpha_i$  complex and, therefore, it is not functional (Dessauer et al. 1998; Van Keulen & Röthlisberger 2017b).

The *apo* ternary complex appears to be stable over the course of 2.1  $\mu\text{s}$  of all-atom MD simulation with a root-mean-square deviation (RMSD) of the complex's backbone fluctuating between 0.8 and 1 nm (Fig. 2B) compared to the first frame of the trajectory. The RMSD of each individual protein, i.e. AC5,  $G\alpha_{\text{olf}}$  or  $G\alpha_i$ , in the *apo* ternary complex remains below 0.4 nm (Fig. S1). Similar RMSD values have been found for the *apo* forms of the binary complexes  $AC5 \cdot G\alpha_{\text{olf}}$  and  $AC5 \cdot G\alpha_i$  (Fig. S1). Additionally, analysis of the secondary structures and calculations of the numbers of H-bonds as functions of time for all systems confirm the overall stability suggested by the RMSD analysis (Fig. S2 – S5). Root-mean-square-fluctuations (RMSF) per residue have also been calculated (Fig. S6).

Minor differences in RMSF were observed for  $G\alpha_{\text{olf}}$  and  $G\alpha_i$ , independently of the simulated system. Conversely, in the case of AC5, the C2  $\beta 4'$ - $\beta 5'$  region (i.e. residues Val1186 to Trp1200 of the C2 domain) and the C2  $\beta 7'$ - $\beta 8'$  region (i.e. residues Gln1235 to Asn1256 of the C2 domain) show a change in orientation dependent on the presence of the  $G\alpha$  subunit. Whereas  $\beta 7'$ - $\beta 8'$  appears to be more flexible in the binary  $AC5 \cdot G\alpha_{\text{olf}}$  complex, the  $\beta 4'$ - $\beta 5'$  region is more flexible in the presence of  $G\alpha_i$ . Besides RMSD, a measure of compactness of the simulated complexes is provided by the global radius of gyration ( $R_g$ ), which also provides an indication of the stability of the complex.  $R_g$  was calculated as a function of time along the simulated trajectories for all three complexes (Fig. S7). In the case of the *apo*  $AC5 \cdot G\alpha_i$  complex, a clear reduction of  $R_g$  can be observed compared to its initial conformation. The *apo* form of  $AC5 \cdot G\alpha_{\text{olf}}$  also shows a reduction of  $R_g$  over time, while  $R_g$  increases for the *apo* ternary complex system.

## **Simulations of the *apo* and *holo* state of the ternary complex indicate that it is unable to catalyse ATP conversion**

To assess the ability of the ternary complex to catalyse the conversion of ATP to cAMP, we investigated the structural dynamics of the ATP

binding site during the MD simulation of the *apo* ternary complex, and the conformations sampled by ATP in a simulation of the *holo* ternary complex,  $G\alpha_{\text{off}} \cdot AC5 \cdot G\alpha_i$  in which ATP is bound to the active site of AC5. We compare the conformational changes of the proteins in the *apo* ternary complex with those in the previously reported simulation of the *apo*  $AC5 \cdot G\alpha_i$  complex (Van Keulen & R othlisberger, 2017b) and with those of the *apo*  $AC5 \cdot G\alpha_{\text{off}}$  simulation reported here.

The ability of AC5 to convert ATP to cAMP depends on the state of its catalytic domain. A characteristic quantity in this respect is the relative distance between the two helices  $\alpha 4'$  and  $\alpha 4$  positioned either side of the binding groove (Fig. 2A). The distance between the C $\alpha$  atom of Thr1007 in helix  $\alpha 4$  and the C $\alpha$  atom of Ser1208 in helix  $\alpha 4'$  (highlighted by the green dashed line in Fig. 2A) was calculated along the simulated trajectories for the three complexes investigated here and reported as function of time in Fig. 2C.

This distance exhibits a clear decrease in the first 100 ns in the  $G\alpha_{\text{off}} \cdot AC5 \cdot G\alpha_i$  complex, starting from a value of 1.9 nm and reaching a stable value of about 1.1 nm. Similarly, a decrease of the  $\alpha 4$ - $\alpha 4'$  distance was also observed in the  $AC5 \cdot G\alpha_i$  complex along 3  $\mu$ s of simulation. Conversely, when AC5 is bound to  $G\alpha_{\text{off}}$  in a binary complex, the distance between the two helices is characterized by a higher value with respect to the case of the  $AC5 \cdot G\alpha_i$  and  $G\alpha_{\text{off}} \cdot AC5 \cdot G\alpha_i$  complexes. A larger value of this distance can be associated with a higher accessibility of the binding groove. On the other hand, a reduced value, as found in the AC5 domain bound to  $G\alpha_i$  implies a lower accessibility to the binding groove. This partial closure of the active site of AC5 in  $AC5 \cdot G\alpha_i$  and  $G\alpha_{\text{off}} \cdot AC5 \cdot G\alpha_i$  reduces the space available for ATP binding, suggesting that the ternary complex likely is inactive.

Apart from the ability of the *apo* ternary complex to bind the substrate, we additionally investigated the possible catalytic activity of a *holo*  $G\alpha_{\text{off}} \cdot AC5 \cdot G\alpha_i$  complex. ATP has to undergo a cyclisation reaction in order to form the products cAMP and pyrophosphate. This reaction is induced by the attack of a deprotonated hydroxyl moiety in ATP's sugar ring, O3\*, on the phosphorus atom of the  $\alpha$ -phosphate moiety (Fig. 2E). Hence, ATP conversion requires oxygen O3\* to be in the proximity of (A)Mg<sup>2+</sup> to which the phosphorus atom is coordinated in order to obtain a conformation that can undergo the cyclisation reaction (Tesmer & Sprang, 1998; Steitz 1993; Nakamura et al. 2012).

A crystal structure of the *holo* AC domain dimer in complex with a stimulatory  $G\alpha$  subunit (Tesmer et al., 1999) shows the active conformation of ATP $\alpha$ -S, an ATP mimic, in the active site of the enzyme in the presence of a  $Mg^{2+}$  ion and a  $Mn^{2+}$  ion (Fig. 2D), which is assumed to be substituted by a second  $Mg^{2+}$  ion under physiological conditions. The O3\*-(A) $Mg^{2+}$  distance in the X-ray structure of the *holo* AC  $\cdot$   $G\alpha_s$  complex is 5.25 Å (Fig. 2D). In the MD trajectory of the *holo* ternary complex, the O3\*-(A) $Mg^{2+}$  distance starts at a similar value and mainly remains in this state for the first 160 ns. Within the first 160 ns, the O3\*-(A) $Mg^{2+}$  distance even decreases to distances as short as 3.7 Å, closer to the distance which has been suggested to correspond to ATP's reactive state (Tesmer & Sprang; 1998, Steitz 1993; Nakamura et al. 2012) (see orange line). However, after 160 ns, the ATP molecule undergoes a drastic conformational change, resulting in an increase of the O3\*-(A) $Mg^{2+}$  distance to  $\approx$  6.5 Å. In this state, the ATP molecule is unable to attain a short O3\*-(A) $Mg^{2+}$  distance, such as observed at 41 ns, which is a feature of the reactive state of ATP. This conformational transition of ATP appears to be irreversible on the  $\mu$ s time scale, thus suggesting the inhibition of the catalytic reaction.

### **The rate of diffusional association of each $G\alpha$ protein subunit to AC5 is unaffected by prior binding of the other subunit**

To provide initial values for the forward rate constants - the parameters in the kinetic model of AC5 activity which were not constrained experimentally - we performed BD simulations (Table 1). The predicted rate constants suggest both  $G\alpha$  subunits form complexes at similar rates, and their association is not greatly affected by the presence of ATP in the AC5 active site, or prior binding of the other subunit. Indeed, the variation in the predicted rate constants for each reaction across the different MD snapshots used in BD simulations is greater than the variation of the mean values for each constant (Table S1).

It should be noted that the predicted rate constants are for the diffusional approach and initial binding of the  $G\alpha$  subunits to AC5. The previously reported MD simulations (Van Keulen & Röthlisberger, 2017b) show that the binding of  $G\alpha_{\text{off}}$  to AC5  $\cdot$   $G\alpha_i$  is hindered by a conformational change of its binding groove on AC5, adding an additional conformational gating contribution to the rate of binding that is not described by the BD simulation method used.



## The presence of an inactive ternary complex improves the ability of the network to detect coincident signals

We incorporated the results from the MD and BD simulations into a kinetic model of the AC5 signal transduction network, the basic feature of which is a regulatory scheme where the ternary complex can form (Fig. 3C). We find that this network can perform coincidence detection. To investigate how the ternary complex contributes to the network's ability to perform coincidence detection, we compared the system with a network in which no ternary complex can form.

It is important to note that there are two aspects of coincidence detection: (a) distinguishing between the different inputs, and (b) responding strongly enough with an increase in cAMP concentration that is physiologically relevant. As a proxy for the amount of cAMP produced, we use the average catalytic rate of AC5,  $k_c$ , since the amount of cAMP produced is proportional to  $k_c$  (see Methods, and also illustrated in Fig. 3). The average catalytic rate of AC5 is a weighted average of the catalytic rates of the unbound enzyme and each of the complexes with the  $G\alpha$  subunits. Additionally, to measure whether the signal transduction network distinguishes between the different input situations, the synergy quantity,  $S$ , is employed. This describes how much greater the average catalytic rate is when both signals coincide compared to the cases when only one of them arrives (see Methods). A synergy value greater than 1 indicates that the network can perform coincidence detection, i.e. the network responds more strongly when the two signals coincide than if each of them occurs individually and are summed. A value of 1, or less than 1, marks a response equal to or weaker than for the sum of the individual signals, respectively. In these cases, the average catalytic rate does not produce distinguishable amounts of cAMP that enable the cell to discriminate between the different input situations. Since a synergy greater than 1 does not necessarily indicate a strong response from the network (which could happen if the basal AC5 catalytic rate is very low), a combination of the average catalytic rate and the synergy is applied where needed to quantify coincidence detection (see the metric C in methods).

The regulatory schemes that we compare are given in Figs. 3B and 3C. We name the first scheme an *allosteric exclusion scheme* – the binding of one  $G\alpha$  subunit excludes the possibility for binding of the other  $G\alpha$  subunit. The second scheme is termed the *simultaneous binding scheme*, where both  $G\alpha$  subunits can bind to AC5 and the ternary complex can be formed. Simulation results for both schemes are given in Fig. 3. The inputs are assumed to be a dopamine peak of 0.5s (Da  $\uparrow$ ) and an acetylcholine dip of 0.5s (ACh  $\downarrow$ ), and the corresponding

rise in  $G\alpha_{\text{olf}}$  and drop in  $G\alpha_i$  are shown in Fig. 3A. Time courses showing the amounts of all AC5 species (the free enzyme and the complexes with the  $G\alpha$ ) are given in Fig. S8.

The simultaneous binding scheme can better distinguish between  $\text{Da} \uparrow + \text{ACh} \downarrow$  and the individual signals  $\text{Da} \uparrow$  or  $\text{ACh} \downarrow$ , it has higher synergy. Both the schemes have a similar maximal  $k_c(\text{Da} \uparrow + \text{ACh} \downarrow)$ , and, as evident, the increase in synergy in the simultaneous binding scheme versus the allosteric exclusion scheme comes from a reduced  $k_c(\text{Da} \uparrow)$ . This relative difference in the average catalytic rate enables the simultaneous binding scheme to respond differently to the coincident signal ( $\text{Da} \uparrow + \text{ACh} \downarrow$ ) compared to  $\text{Da} \uparrow$  alone, as is also visible from the amounts of cAMP produced, and hence to differentiate between the two input situations. The allosteric exclusion scheme, on the other hand, produces similar values for  $k_c(\text{Da} \uparrow + \text{ACh} \downarrow)$  and  $k_c(\text{Da} \uparrow)$  and thus responds similarly to  $\text{Da} \uparrow + \text{ACh} \downarrow$  and to  $\text{Da} \uparrow$  alone, being unable to distinguish well between them in terms of cAMP production. The reason for this is the exclusivity of the interaction between each of the  $G\alpha$  proteins and AC5: when only  $\text{Da} \uparrow$  arrives,  $G\alpha_{\text{olf}}$  is able to compete with  $G\alpha_i$  and bind to much of the enzyme (approximately half of it as shown in Fig. S8B). This creates the catalytically active complex  $\text{AC5} \cdot G\alpha_{\text{olf}}$ , driving an increase in  $k_c(\text{Da} \uparrow)$ . In this case, reduced inhibition of AC5 by an additional  $\text{ACh} \downarrow$  does not contribute much to  $k_c(\text{Da} \uparrow + \text{ACh} \downarrow)$ . In the simultaneous binding scheme, however, a  $\text{Da} \uparrow$  causes the formation of the ternary complex (Fig. S8F), and due to its inactivity  $k_c(\text{Da} \uparrow)$  does not increase significantly. Only with an additional  $\text{ACh} \downarrow$  is the inhibition by  $G\alpha_i$  relieved and the proportion of the active complex  $\text{AC5} \cdot G\alpha_{\text{olf}}$  is increased, enabling a high  $k_c(\text{Da} \uparrow + \text{ACh} \downarrow)$ . Importantly,  $k_c(\text{Da} \uparrow)$  is also low for an inactive ternary complex so that little cAMP is produced with a  $\text{Da} \uparrow$  only and little "stray" activation of downstream signalling would occur. In fact, only for a substantially active ternary complex does the simultaneous binding scheme become comparable to the allosteric exclusion scheme in terms of synergy (Figs. 3D, 3E, and 3F). For a wide range of low to moderate ternary complex activity, it performs coincidence detection better. The maximum of the catalytic rate is not affected much by the activity of the ternary complex (Fig. 3E), and the metric C shows that coincidence detection is most significant for an inactive ternary complex (Fig. 3F). An inactive ternary complex enables the lowest basal catalytic activity of the enzyme and hence the biggest difference between  $k_c(\text{Da} \uparrow)$  and  $k_c(\text{Da} \uparrow + \text{ACh} \downarrow)$ , and this in turn maximizes the synergy.

In the supplementary material we show that the allosteric exclusion



scheme in itself lacks the ability to perform coincidence detection, and this is due to the exclusivity of the regulatory interaction. Coincidence detection with this scheme, as demonstrated in Fig. 3B, is in fact a result of the amounts of  $G\alpha_{\text{off}}$  and  $G\alpha_i$  and the kinetics determined by the forward rate constants.

An inherent property of a coincidence detector is that there exists a time window over which two signals can be detected as if arriving together. The detector uses some mechanism by which it “remembers” the occurrence of one of the signals for some time interval, and responds when the other signal arrives within this interval. For the AC5 signal transduction network, the existence of the detection window also depends on the regulatory scheme. In fact, the formation of the ternary complex is very important to allow for a broader window of coincidence detection. In the case of only a  $Da \uparrow$ , a ternary complex that has buffered (or absorbed) the elevated active  $G\alpha_{\text{off}}$  provides this memory: allowing the  $ACh \downarrow$  to arrive some time later and still elicit a response (Fig. 3G). This is potentially relevant, since the cholinergic interneurons responsible for the  $ACh \downarrow$  have been found to produce a second  $ACh \downarrow$  to certain stimuli (Zhang and Cragg, 2017). The length of the detection window is determined by the rate of deactivation of the active  $G\alpha_{\text{off}}$  (also illustrated in Figs. S9D and S9G, and is due to the fact that the GTPase activity for  $G\alpha_{\text{off}}$  is lower than the one for  $G\alpha_i$ ). Both schemes technically have the same length of detection windows, but the allosteric exclusion scheme has a high synergistic effect in a very narrow region of the window - the signals need to occur practically simultaneously (Fig. 3G). The detection window is asymmetric, i.e. the  $Da \uparrow$  needs to arrive first to elicit a response from the network. (Time courses with  $ACh \downarrow$  preceding and following a  $Da \uparrow$  illustrating the difference between the two schemes are given in Fig. S9.)

Lastly, we note that a critical aspect for coincidence detection to work is to have fast deactivation of the active  $G\alpha_i$ . Then the dynamics of  $G\alpha_i$  inside the cell can follow the short duration of the  $ACh \downarrow$  signal. The experimental evidence for this high GTPase rate is listed in the description of the kinetic model (see Methods). The effect of the GTPase rate on coincidence detection is shown in Fig. S10. There is an optimum value of this rate - it needs to be both high enough to cause a drop in  $[G\alpha_i]$  during the  $ACh \downarrow$  and low enough so that there is significant inhibition of AC5 at steady state. Since the deactivation of  $G\alpha_i$  is faster than that for  $G\alpha_{\text{off}}$ , then, provided there is enough active  $G\alpha_{\text{off}}$  to bind to AC5, the duration of the synergistic effect is determined by the duration of the pause (Fig. S9E and S9H).

To summarize, the results of this section show that the formation of the ternary complex aids coincidence detection and prolongs the detection window. Additionally, the less catalytically active the ternary complex is, the better the coincidence detection. As elaborated in the discussion, an inactive ternary complex can also explain recent experimental results on cAMP production due to activation of the implicated GPCRs in the native system (Yapo et al., 2017; Nair et al., 2019).

## **Hindrance of $G\alpha_{\text{off}}$ binding to $AC5 \cdot G\alpha_i$ further increases coincidence detection**

To see where the predicted values from the BD simulations lie in terms of affecting coincidence detection, we performed parameter scans for the values of the forward rate constants. All of the forward rate constants affect the synergy, since they affect the fractions  $q_i$ ,  $i = 1, \dots, 4$ , of each species at any point in time (see equations for  $q_i$  in Methods).

To begin with, we address the observation from Van Keulen and Röthlisberger (2017b) that the  $G\alpha_{\text{off}}$  binding groove in  $AC5 \cdot G\alpha_i$  adopts a conformation that hinders  $G\alpha_{\text{off}}$  binding. This could further decrease the value of the rate constant  $k_{f4}$ , compared to the value predicted in the BD simulations. We investigated the effect such a decrease has on coincidence detection by altering  $k_{f4}$  by varying orders of magnitude (Figs. 4A, 4B, and 4C). We found that hindered binding of  $G\alpha_{\text{off}}$  to  $AC5 \cdot G\alpha_i$  increases the synergy  $S$  by 12%. For this reason, when performing the parameter scans, we considered two scenarios. In the first one, we used  $k_{f1} = k_{f4}$  and  $k_{f2} = k_{f3}$  since the BD simulations showed that these values are similar, at least in order of magnitude. In the second scenario, we used  $k_{f2} = k_{f3}$  and  $k_{f4} = k_{f1}/100$ . We call this scheme, in which the reaction corresponding to the rate  $k_{f4}$  is slower, the *hindered simultaneous binding scheme*.

For the simultaneous binding scheme, a very wide range of tested values for  $k_{f1}$  provides similar  $k_c$  and synergy values for a given  $k_{f2}$  (Figs. 4D and 4E), which can be interpreted as follows. Similarly to the requirement for a high GTPase activity for  $G\alpha_i$ , it is necessary that  $G\alpha_{\text{off}}$  binds to  $AC5$  quickly enough to be able to follow the signal  $Da \uparrow$ . Since active  $G\alpha_{\text{off}}$  has a slower dynamics than the input  $Da \uparrow$ , i.e.  $G\alpha_{\text{off}}$  exists inside the cell for some time after the outside signal has stopped, it is likely that a range of values for the rate constant  $k_{f1}$  can enable coincidence detection (not only values that match the length of a  $Da \uparrow$ , which are around  $k_{f1} = 2 \text{ (nMs)}^{-1}$  for a  $Da \uparrow$  of 0.5s). The

synergy grows with  $k_{f1}$  since a higher binding rate of  $G\alpha_{olf}$  provides a higher maximum of  $k_c$  during the  $Da \uparrow + ACh \downarrow$ , whereas  $k_c(Da \uparrow)$  is not affected much (Figs. S11A and S11B).

Increasing the rate constants  $k_{f2} = k_{f3}$  for  $G\alpha_i$  binding also causes an increase in synergy. The lower these constants, the less inhibited the enzyme will be due to smaller fractions of both  $AC5 \cdot G\alpha_i$  and  $G\alpha_{olf} \cdot AC5 \cdot G\alpha_i$ . This allows for more stimulation by the available  $G\alpha_{olf}$  and hence a higher basal  $k_c$  and a higher  $k_c(Da \uparrow)$ . The situations  $Da \uparrow + ACh \downarrow$  and only  $Da \uparrow$  produce a more similar response, and hence show a lower synergy. Higher values for  $k_{f2} = k_{f3}$ , on the other hand, allow for both stronger basal inhibition of AC5 and more ternary complex formed, and hence a lower basal  $k_c$  and lower  $k_c(Da \uparrow)$ , thus increasing the synergy. The region of optimal parameters for the simultaneous binding scheme is quite wide in terms of  $k_{f1} = k_{f4}$  and  $k_{f2} = k_{f3}$ , and the most optimal scenario is for the largest values tested, as shown in Fig. 4F using the metric  $C$ .

Compared to the simultaneous binding scheme, the hindered simultaneous binding scheme does not affect the maximum of the average catalytic rate significantly (Fig. 4H), but it does increase the synergy and move the region of optimal values towards low values for the rate constant  $k_{f1}$  (Fig. 4G). Inspecting the dynamics of the model with this regulatory scheme reveals the reason: the hindered reaction  $AC5 \cdot G\alpha_i + G\alpha_{olf} \leftrightarrow G\alpha_{olf} \cdot AC5 \cdot G\alpha_i$  causes less ternary complex to be formed and consequently less  $AC5 \cdot G\alpha_{olf}$  from the dissociation of  $G\alpha_i$  from the ternary complex (the route via  $k_{f3}$ ) (Figs. S11C and S11D). This, in general, lowers  $k_c(Da \uparrow)$  compared to the simultaneous binding scheme, creating a larger relative difference between  $k_c(Da \uparrow)$  and  $k_c(Da \uparrow + ACh \downarrow)$  which results in a high synergy. This difference is largest for low values of  $k_{f1}$  and decreases with  $k_{f1}$  due to the higher amounts of  $AC5 \cdot G\alpha_{olf}$  during the  $Da \uparrow$  (higher  $k_c(Da \uparrow)$ ). Importantly, the maximal  $k_c$  has the opposite dependence on  $k_{f1}$  from the synergy, so that the region of values for  $k_{f1}$  optimal for coincidence detection optimizes between a high catalytic rate and a high synergy (Fig. 4I). The effect of  $k_{f2} = k_{f3}$  on coincidence detection is the same as described for the simultaneous binding scheme.

In both scenarios, the predictions of the BD simulations are favourable for coincidence detection. However, and this is particularly prominent for the hindered simultaneous binding scheme (Fig. 4I), higher binding rates of  $G\alpha_i$  than the predicted ones are better suited for coincidence detection. This increase in  $k_{f2}$  and  $k_{f3}$  could be provided by the tethering to the membrane due to the myristoyl moiety in  $G\alpha_i$ .

Additionally, this increase could arise if  $G\alpha_i$  were part of multiprotein signaling complexes, as has been shown for AC5 and  $G\alpha_{olf}$  (Cooper 2003; Cooper and Crosswaithe 2006; Xie et al. 2015).

## Discussion

In this study we find that an inactive ternary complex between AC5 and its G protein regulators, a molecular-level feature, gives rise to coincidence detection, a systems-level function of the signal transduction network that AC5 is embedded in. In order to investigate the stability and the activity of the putative  $G\alpha_{olf} \cdot AC5 \cdot G\alpha_i$  ternary complex, we carried out all-atom MD simulations. Our results showed that on the  $\mu s$  time scale, the complex seems to be stable independently of the presence or absence of ATP. Additionally, previous MD studies suggest possible pathways for the formation of the ternary complex, showing the possibility of the  $G\alpha_i$  protein to bind to the *holo*  $AC5 \cdot G\alpha_s$  complex (Frezza et al. 2018), and disfavoring the binding of  $G\alpha_{olf}$  to the *apo*  $AC5 \cdot G\alpha_i$  complex (Van Keulen & R othlisberger 2017b). Overall, it should be pointed out that MD simulations cannot exclude the instability of the ternary complex on longer time scales, which cannot be assessed due to computational limits. However, MD simulations can help us to investigate the conformations sampled by the ternary complex at physiological temperature and pressure and, consequently, the activity of the complex. Indeed, the partial closure of the binding groove found in the *apo* ternary complex, analogous to that occurring in the binary *apo*  $AC5 \cdot G\alpha_i$ , suggests a lack of catalytic activity in the ternary complex due to the reduced accessibility for the ATP substrate. Additionally, even if a ternary complex could exist with ATP bound to AC5, our results show that the substrate would adopt a conformation not suitable for the subsequent catalytic reaction leading to the formation of cAMP. It is worth mentioning that possible conformations sampled by ATP, prior and during its conversion to cAMP, have been reported by Hahn et al. (2015) in a theoretical study. Such conformations, required for an optimal conversion of ATP to cAMP, clearly show an opposite orientation of the oxygen O3\* with respect to that sampled in our simulation, thus supporting our hypothesis about the inactivity of the ternary complex. Recently, experimental studies with the *in vitro* native system have been performed (Nair et al. 2019; Yapo et al. 2017). In  $D_1$  MSNs, stimulating the  $D_1$  receptors with an agonist followed by activation of the  $M_4$  receptors completely abolishes the cAMP response of AC5 (Nair et al., 2019, Fig. 3A). This is consistent with an existing and inactive ternary complex, since under these conditions both active  $G\alpha_{olf}$  and active  $G\alpha_i$  would exist in the cell, and activation of  $G\alpha_i$  completely stops the activity of the previously formed  $AC5 \cdot G\alpha_{olf}$ . The analogous experiment in  $D_2$  MSNs is also consistent

with an existing and inactive ternary complex (Yapo et al., 2017, Fig. 2B). Stimulating the  $A_{2a}$  receptor with an agonist and then uncaging dopamine, which stimulates the  $D_2$  receptor, also abolishes the cAMP response. A similar result has been recently obtained in striatal cultures, where stimulating the  $D_2$  receptor almost entirely counteracts the effects of the applied agonist on the  $A_{2a}$  receptor (Navarro et al. 2018). Earlier *in vitro* experiments with membranes of Sf9 cells expressing AC5, however, contradict the results of this study and the experiments in (Nair et al., 2019; Yapo et al., 2017). Adding both  $G\alpha_{\text{olf}}$  and  $G\alpha_i$  to the assays of AC5-containing membranes did not completely inhibit AC5 - the enzyme still produced significant amounts of cAMP (Chen-Goodspeed et al., 2005; Taussig et al., 1994). These results were nevertheless interpreted and fitted with an interaction scheme where the ternary complex can form and it is not very active, and the production of cAMP is due to higher order, catalytically active complexes of AC5 with more than one  $G\alpha_{\text{olf}}$  and  $G\alpha_i$  subunit (Chen-Goodspeed et al., 2005). Lastly, in the recent demonstration of functional oligomeric complexes of AC5 and the  $A_{2a}$  and  $D_2$  a spatial arrangement of the complex is proposed which, importantly, supports ternary complex formation (Navarro et al. 2018). The disruption of such complexes in membrane fragments from Sf9 cells could account for the discrepancy in the experimental results mentioned above. We therefore conclude that the results of our study are plausible and supported by existing experiments with the native system.

## Relevance for corticostriatal synaptic plasticity

Knowing what an intracellular signal transduction network is composed of and the details of how it operates can help to clarify how it responds to extracellular events. The AC5 signal transduction network in  $D_1$  MSNs (as well as in  $D_2$  MSNs) interacts with a calcium-activated signal transduction network to regulate synaptic plasticity. Calcium influx at the synapse is necessary for synaptic potentiation, but exerts its effect only if accompanied activation of the AC5 signaling module (Fino et al., 2005; Pawlak and Kerr, 2008; Shen et al., 2008). Thus, the AC5 signal transduction network gates plasticity in the corticostriatal synapses onto the MSNs. Now, an existing and inactive ternary complex in AC5 regulation has consequences on how this “gate” would be opened: disinhibition from active  $G\alpha_i$  is necessary, accompanied by stimulation from  $G\alpha_{\text{olf}}$ . That is, our findings suggest that experimentally observed  $ACh \downarrow$  in the striatum is likely physiologically relevant for  $D_1$  MSNs, and both a  $Da \uparrow$  and a  $ACh \downarrow$  are necessary to enable synaptic potentiation (see also Fisher et al., 2017). They can also help in interpreting the functional role of the neuromodulatory signals in the striatum.



The kinetic model of the AC5 signal transduction network, built according to the findings of the MD simulations and with the parameters predicted with the BD simulations, reveals improved coincidence detection when compared to alternative regulatory schemes. This, together with the implications mentioned above arising from the existence and inactivity of the ternary complex, suggests that the regulation of AC5 has indeed evolved to perform coincidence detection of the two neuromodulatory signals.

## **Comparisons to other AC isoforms and AC-dependent cascades**

In this study we have investigated the regulation of AC5 through interaction with the  $G\alpha_{\text{off}}$  and  $G\alpha_i$  subunits. All membrane-bound AC isoforms are known to be stimulated by  $G\alpha_s$ , a close homologue of  $G\alpha_{\text{off}}$ , while only ACs 1, 5 and 6 are inhibited by  $G\alpha_i$  (Sadana & Dessauer, 2009). With this in mind, it is interesting to ask whether our findings concerning AC5 regulation, particularly the presence of an inactive ternary complex in the signalling network, could also be valid for cascades containing ACs 1 and 6. The sequences of rat  $G\alpha_s$  and  $G\alpha_{\text{off}}$  are highly similar with an identity of 76.0 % and similarity of 90.0 % (Fig. S12). Restricting the comparison to the amino acid residues within 6 Å of AC5 in the modelled *apo* AC5 ·  $G\alpha_{\text{off}}$  complex, the identity rises to 95.8 %, with only a single position differing. For this reason, it is reasonable to assume that our findings regarding the formation of  $G\alpha_{\text{off}}$ -containing complexes are also applicable to  $G\alpha_s$ . Indeed, our modelling of the AC5 ·  $G\alpha_{\text{off}}$  complexes assumes that we can take crystal structures of AC ·  $G\alpha_s$  complexes as template structures. It should be noted that  $G\alpha_s$  is known to be deactivated more slowly than  $G\alpha_{\text{off}}$  (Lui et al, 2001), which could reduce the ability of  $G\alpha_s$ -activated networks to detect subsecond coincident signals (see Nair et al., 2015).

Previously, we have performed electrostatic analyses of mouse AC isoforms, to identify regions of electrostatic similarity within similarly regulated isoforms (Tong et al, 2016). In that work, we showed that the molecular electrostatic potentials surrounding ACs 1, 5 and 6 in aqueous solution were very similar in the  $G\alpha_i$  binding region of AC5, suggesting that the location of binding, and the bound orientation, of  $G\alpha_i$  on ACs 1 and 6, could be similar. This electrostatic similarity was due to a more negative character, compared to other AC isoforms, which is complementary to the largely positive potential of the face of  $G\alpha_i$  that contains the switch II region that is thought to interact with AC.

The sequence identities of AC isoforms with respect to AC5, in the C1 domain to which  $G\alpha_i$  binds, show that ACs 1 and 6 are most similar, at 73.5 % and 94.7 %, respectively (Fig. 5B). Considering only those residues predicted to be involved in the interaction with  $G\alpha_i$ , the similarities are 64.7 % and 91.2 %. From the very high electrostatic and sequence similarity, it seems reasonable to assume that our findings should hold for AC6.

While AC1 is inhibited by  $G\alpha_i$ , the level of inhibition is much lower, with higher levels only seen for its forskolin or calmodulin-activated states (Taussig et al, 1992), therefore directly applying our findings to AC1 cascades is more difficult. In the AC1 C1 domain sequence, there are three charge-altering substitutions in the region formed by the C-terminal end of  $\alpha 3$ -helix and the loop connecting this helix to the  $\beta 4$ -strand (Fig. 5C). These substitutions give this region a more negative character, and therefore it is reasonable to assume that they should not destabilize the binding mode we find for  $G\alpha_i$  on AC5 to a large extent. In a previous mutagenesis study (Dessauer et al, 1998), including one of these substitutions (N559D by Uniprot sequence, N480D by sequence in (Dessauer et al, 1998)), which is also present in the non- $G\alpha_i$  inhibited ACs 2, 4, 7 and 8 (Fig. S13), as a mutation in AC5 was found to produce only a small reduction in its inhibition by  $G\alpha_i$  (less than 2-fold increase in IC50). A more significant effect on the binding of  $G\alpha_i$  to AC1 may occur due to a difference in the C-terminal residue of the  $\alpha 3$ -helix of the C1 domain. In AC1, there is an alanine in this position, while in ACs 5 and 6, it is a valine. The wild-type AC5 construct used by Dessauer et al. differed from the canonical sequence by having a methionine in this position (476 by their sequence numbering, 555 in the Uniprot sequence). They showed that mutating this residue to match the canonical sequence reduced the IC50 of  $G\alpha_i$  by a third, while mutation to alanine gave a greater than 30-fold increase in IC50. Due to this apparent reduction in the affinity of AC1 for  $G\alpha_i$ , further MD simulations may be required to confirm the stability of a  $G\alpha_{off} \cdot AC1 \cdot G\alpha_i$  ternary complex. The lower sequence similarity between the C1 domains of ACs 1 and 5 also suggests that the allosteric effects on both the  $G\alpha_{off}/G\alpha_s$  binding groove and the active site could be different in a putative AC1 ternary complex. Again further MD simulations would be required to investigate this, as well as to further unravel the different computational properties of the AC isoforms found in different synapses.

## Assumptions and limitations

As for any simulation study aimed at investigating *in vivo* subcellular processes, there are limitations that should be discussed. First, adenylyl cyclases, together with other components of the signal transduction networks they participate in, are organized as parts of multiprotein signaling complexes and/or are localized in structured microdomains in the cell which serve to compartmentalize the effects of the produced cAMP and efficiently activate downstream components of the networks and, ultimately, effectors (Cooper 2003, Cooper and Crosswaithe 2006, Xie et al. 2015, Dessauer 2009, Navarro et al. 2018). The kinetic model here, on the other hand, assumes mass-action kinetics for the species included, i.e. it disregards any organization into multiprotein signaling complexes and instead describes a well-mixed solution of molecular species. This means that it reproduces the experimental measurements on cAMP in a partly phenomenological way. For example, AC5 needs to be presented with appropriate proportions of  $G\alpha_{\text{olf}}$  and  $G\alpha_i$  to reproduce the levels of cAMP, which may not necessarily be the same as the amounts of these proteins in real synapses. Second, a recent study has demonstrated that AC5 and the heterotrimeric  $G_{\text{olf}}$  protein are pre-assembled into a signaling complex and suggested that upon activation by the GPCR, the  $G\alpha_{\text{olf}}$  subunit rearranges rather than physically dissociates from the  $G\beta\gamma$  subunit (Xie et al. 2012). This would imply an increase in the forward rate constant for AC5 and  $G\alpha_{\text{olf}}$  binding predicted with the BD simulations. In light of this study, the effect of the hindered  $G\alpha_{\text{olf}}$  binding to  $AC5 \cdot G\alpha_i$  is not clear, since its main advantage of improving coincidence detection occurs precisely for values of  $k_{f1}$  around the BD estimates. It remains to be seen how much of an increase in the forward rate constant pre-assembly confers. A similar situation likely occurs for  $G\alpha_i$ , as well - the GPCRs and AC5 form oligomeric complexes that could include the G proteins (Navarro et al. 2018), which would mean that the predicted value for the forward rate constant for AC5 and  $G\alpha_i$  binding,  $k_{f2}$ , is also probably an underestimate. At the very least, the membrane anchoring of  $G\alpha_i$  by the myristoyl moiety would result in an increase in  $k_{f2}$ . A larger value for  $k_{f2}$  is beneficial for coincidence detection both with the simultaneous and the hindered simultaneous binding scheme (Figs. 4G-I). Finally, we should underline that the enzyme is additionally regulated by protein kinase A (PKA), calcium ions, nitric oxide, and the  $G\beta\gamma$  subunit, and regulation via the transmembrane domains has been proposed (but not demonstrated so far) (Cooper 2003, Brand et al. 2015, Linder 2006). PKA is activated by cAMP and is the most common kinase to elicit the various downstream responses of the signal transduction network. PKA also inhibits AC5 via phosphorylation, and this is probably feedback that serves for signal termination. Calcium also inhibits AC5, an interaction which, due to



excitatory synaptic input, might also help terminate its activity. The  $G\beta\gamma$  enhances the effect of  $G\alpha_s$  on AC5, but has no effect alone, and nitric oxide has an inhibitory effect whose purpose is also unknown. The measures for coincidence detection used here do not include these additional regulatory interactions, and this would provide a more complete picture of the enzyme's regulation in studies of various signaling scenarios.

Furthermore, concerning the structural simulations carried out in the present study, it is appropriate to highlight some aspects. First, while the *apo* and the *holo* ternary complexes are relatively stable over about 2.1 and 1.1  $\mu$ s of MD simulation time, respectively, we cannot exclude that on a longer time scale such complexes could show a dissociation of the different protein units. In this regard, it is worth mentioning that both simulations of the *apo* and *holo* forms of the ternary complex have been repeated starting with new velocities for about 0.6 and 1.0  $\mu$ s, respectively, leading to the same overall conclusions described above. Second, in the systems simulated here, only the catalytic domains of AC5 are considered, while the transmembrane domains are not included. Although the transmembrane domains are important for the proper dimerization of the catalytic domains (Seebacher et al. 2001), the functionality of AC5 was experimentally found to be maintained upon removal of the transmembrane domains (Dessauer, et al. 1998; Whisnant, et al. 1996). At present, it is not possible to include the transmembrane domains in an MD simulation both because their structure has not yet been resolved and because such a simulation would be very computationally expensive. The membrane-anchoring is also neglected in the BD simulations in which freely diffusing solutes are assumed. This assumption has two main effects on the predicted association rate constants, which alter the predictions in opposite directions, leading to some degree of cancellation of errors. The anchoring of AC5 and  $G\alpha_{\text{off}}$  in the membrane would add additional diffusional constraints that would potentially increase rates *in vivo*, by reducing the search space, while the slower diffusion of the lipid anchor in the membrane would slow down association. It should also be noted that the simulated systems have been built by homology modelling using available X-ray crystal structures of AC as described in the Methods section and also reported in previous studies (Van Keulen & Röthlisberger, 2017a; Van Keulen & Röthlisberger, 2017b).

## Conclusions

In this work, we have investigated the stability and activity of a  $G\alpha_{\text{off}} \cdot AC5 \cdot G\alpha_i$  ternary complex by MD simulation and found that the complex appears to be stable on the microsecond time scale, but is unable to catalyze ATP conversion. Using BD simulations, we have made predictions of the association rate constants for the formation of both binary  $AC5 \cdot G\alpha$  complexes, and the subsequent association of the second  $G\alpha$  subunit to form the ternary complex.

Kinetic modelling of the AC5 signal transduction network showed that the predictions of the structure-based simulations maximize the ability of the network to recognize coincident neuromodulatory signals, with coincidence detection enhanced by both the presence of the ternary complex, and its reduced activity. Additionally, coincidence detection is enhanced by the hindered binding of  $G\alpha_{\text{off}}$  to the the binary  $AC5 \cdot G\alpha_i$  complex, as suggested by our previous MD study (Van Keulen & Röthlisberger, 2017b). Taken together, these results provide evidence that AC5 has evolved to perform coincidence detection of transient changes in the amounts of  $G\alpha_{\text{off}}$  and  $G\alpha_i$  proteins, such that a brief deactivation of the  $G\alpha_i$  signaling branch is needed to gate the  $G\alpha_{\text{off}}$  signal through. For the corticostriatal synapse on  $D_1$  MSNs, this implies that both the transient rise in dopamine and the decrease in acetylcholine levels are necessary to trigger synaptic plasticity.

## Methods

### Modelling of Binary AC5 Complexes

The crystal structure (PDB ID 1AZS) of the ATP-free  $AC \cdot G\alpha_s$  complex (Tesmer et al., 1997) was used as a template for the catalytic region of AC5 and  $G\alpha_{\text{off}}$  in the *apo* ternary complex. The template used for the initial complex conformation included 1AZS's C1 and C2 domains (more specifically, canine AC5 for C1 and rat AC2 for C2) for modelling the AC5 structure (UniprotKB Q04400) from *Rattus norvegicus* as well as the  $G\alpha_s$ ' structure for the initial  $G\alpha_{\text{off}}$  (UniprotKB P38406) conformation from *Rattus norvegicus* (Eswar et al., 2006; Marti-Renom et al., 2000; Tesmer et al., 1997). The modelled structure of the myristoylated *Rattus norvegicus*  $G\alpha_i$  subunit (UniprotKB P10824) interacting with guanosine-5'-triphosphate (GTP) and  $Mg^{2+}$  was taken from Van Keulen & Röthlisberger (2017a).  $G\alpha_i$  also has several isoforms, and the one referred to here is  $G\alpha_{i1}$ . Myristoylation is a post-translational modification of the N-terminus of  $G\alpha_i$  that results in the covalent attachment of a 14-carbon saturated fatty acid to the N-terminal glycine residue of  $G\alpha_i$  via an amide bond. The modelled AC5

and  $G\alpha_i$  structures were used for docking  $G\alpha_i$  on AC5's C1 domain to finalise the initial conformation of the ternary complex. This *apo* ternary complex setup was also used to simulate the *apo* forms of AC5 ·  $G\alpha_i$  and AC5 ·  $G\alpha_{\text{olf}}$  by removing the subunit not to be considered.

The crystal structure (PDB ID 1CJK) of the catalytic AC domains with a bound ATP analogue (Adenosine-5'-*rp*-alpha-thio-triphosphate), ATP $\alpha$ S, and a  $G\alpha_s$  interacting with the AC protein, was used as a template for the *holo* ternary complex. The template used for modelling the active AC5 (UniprotKB Q04400) conformation in the ternary complex included the C1 and C2 domains from the PDB file 1CJK (Eswar et al., 2006; Marti-Renom et al., 2000; Tesmer et al., 1999). The  $G\alpha_s$  subunit present in 1CJK was used as a template for the initial  $G\alpha_{\text{olf}}$  (P38406) structure from *Rattus norvegicus* (Eswar et al., 2006; Marti-Renom et al., 2000; Tesmer et al., 1991). The modelled structure of the myristoylated *Rattus norvegicus*  $G\alpha_i$  subunit (UniprotKB P10824) interacting with GTP and  $Mg^{2+}$  was taken from Van Keulen & Röthlisberger (2017a). The active myristoylated *Rattus norvegicus*  $G\alpha_i$  is referred to simply as  $G\alpha_i$  because only a myristoylated form of  $G\alpha_i$  was used in all simulations.

## Modelling of Ternary AC5 Complexes

Membrane-bound ACs consist of two membrane-bound regions and two cytosolic domains. The latter form the active site of the enzyme and its structure has been determined by crystallography. The catalytic domains, C1 and C2, are located close to the membrane due to AC5's transmembrane domains, but remain entirely solvated. The crystal structure templates, used for modelling the complexes, were employed to determine the orientation of  $G\alpha_{\text{olf}}$  on the C2 domain. The HADDOCK web server (de Vries et al., 2010) was used for docking ten conformations of the active  $G\alpha_i$  subunit to AC5's catalytic domains in the *apo* and *holo* forms as described in Van Keulen & Röthlisberger (2017b). The active region of  $G\alpha_i$  was defined in HADDOCK as a large part of the alpha helical domain (112-167), the switch I region (175-189) and the switch II region (200-220), allowing for a large unbiased area on the  $G\alpha_i$  protein surface to be taken into account during docking. The active region of AC5's C1 domain was defined as the  $\alpha$ 1 helix (479-490) and the C-terminal region of the  $\alpha$ 3 helix (554-561) because experimentally it has been found that  $G\alpha_i$  is unable to interact with C2 and its main interactions with AC5 are with the C1 domain (Dessauer et al., 1998). Ten snapshots of  $G\alpha_i$  were used for docking the  $G\alpha$  subunit to the catalytic domain of AC5. These snapshots were extracted at time intervals of 0.5 ns from the end of the classical MD trajectory of  $G\alpha_i$  (around 1.9  $\mu$ s) described in Van Keulen & Röthlisberger (2017a). The same three criteria for complex selection as in Van Keulen & Röthlisberger (2017b) were applied: (1) the absence of

overlap between the C2 domain and  $G\alpha_i$ , (2) no overlap with the GTP binding region of  $G\alpha_i$  and the C1 domain of AC5, and (3) presence of similar complexes in the top-ten docking results of the docking calculations performed for all ten used  $G\alpha_i$  conformations.

## Classical Molecular Dynamics Simulations

The Gromacs 5.1.2 software (Bekker et al., 1993; Abraham et al., 2015) was used to perform the simulations. The *apo* and *holo*  $G\alpha_{\text{olf}} \cdot AC5 \cdot G\alpha_i$  systems, which were simulated for 2.1  $\mu\text{s}$  and 1.2  $\mu\text{s}$  respectively, each include two GTP molecules. In addition, the *holo* complex incorporates four  $\text{Mg}^{2+}$  ions and one ATP molecule, while in the *apo* form only three  $\text{Mg}^{2+}$  ions are present. Both *apo* and the *holo* systems were solvated in about 162,000 water molecules and 150 mM KCl. They were simulated at a temperature of 310 K and a pressure of 1 bar, maintained using the Nosé-Hoover thermostat and an isotropic Parrinello-Rahman barostat, respectively. The force fields used for the protein and the water molecules were AMBER99SB (Hornak et al., 2006) and TIP3P (Jorgensen et al., 1983). For GTP and ATP, the force field generated by Meagher et al. (2003) was used. The adjusted force field parameters for  $\text{Cl}^-$  and  $\text{K}^+$  were taken from Joung *et al.* (2008). The  $\text{Mg}^{2+}$  parameters originated from Allnér *et al.* (2012) and the parameter set for the myristoyl group was taken from reference (Van Keulen & Röthlisberger, 2017a). Electrostatic interactions were calculated with the Ewald particle mesh method with a real space cutoff of 12Å. The van der Waals interactions also had a cutoff of 12 Å. Bonds involving hydrogen atoms were constrained using the LINCS algorithm (Hess 2008). The integration time step was set to 2 fs.

The *apo* binary complexes,  $AC5 \cdot G\alpha_i$  and  $AC5 \cdot G\alpha_{\text{olf}}$ , used for comparison to the ternary complexes, were built via the same procedure and were each simulated for 3  $\mu\text{s}$ .

The first step in the equilibration procedure of the protein systems included the energy minimisation of the protein complex together with the ligands ( $\text{Mg}^{2+}$ , GTP, ATP), referred to as the complete complex. Position restraints of 1000  $\text{kJ mol}^{-1} \text{nm}^{-2}$  were applied to the structure of the complete complex during energy minimisation. The next step that was performed was the simulation of the complete complex under canonical NVT (constant number of atoms (N), constant volume (V) and constant temperature (T)) conditions, starting from the energy minimised structure, with position restraints of 1000  $\text{kJ mol}^{-1} \text{nm}^{-2}$  on the complete complex. The length of the NVT run was 2 ns. The third step included the performance of a 4 ns isothermal-isobaric NPT run (constant number of atoms (N), constant pressure (P) and constant

temperature (T)) with position restraints of  $1000 \text{ kJ mol}^{-1} \text{ nm}^{-2}$  on the complete complex. The fourth step was an NPT simulation of 4 ns, with position restraints of  $1000 \text{ kJ mol}^{-1} \text{ nm}^{-2}$  on the complete complex except for the hydrogens of the proteins. The fifth step contained an NPT run of 4 ns in which the backbone of the proteins were restrained by  $1000 \text{ kJ mol}^{-1} \text{ nm}^{-2}$  as well as the ligands. The sixth step was an unrestrained NPT simulation of at least 10 ns, which was prolonged depending on the RMSD convergence of the proteins in the equilibrated system.

## Forward Rate Constant Estimation via Brownian Dynamics Simulations

Brownian dynamics (BD) simulations were performed to estimate the forward association rate constants in the two schemes in Fig. 3. The simulations were performed using the SDA 7 software package (Martinez et al, 2015), with the associating species represented in atomic resolution as rigid bodies. The inter-species interactions were modeled using the effective charge model (Gabdouline & Wade, 1996), with the electrostatic desolvation term described by Elcock et al. (1999), and following the parameterization of Gabdouline and Wade (2001).

The atomic structures of the reactant species in the forward reactions shown in Figs. 3B and 3C were taken from clustered snapshots of the MD simulations described above, except for the structures of *apo* AC5 and  $G\alpha_i$  used to calculate  $k_{f2}$ , which were obtained from simulations performed by Van Keulen and Röthlisberger (2017b). The electrostatic potential of each snapshot of the reactant species was calculated via solution of the linearized Poisson-Boltzmann equation (PBE) using the APBS PBE solver (Baker et al, 2001), such that at the grid boundaries, the electrostatic potentials matched those of atom-centered Debye-Hückel spheres. The atomic charges of the protein residues were taken from the Amber force field, with the charges of the myristoyl moiety as described by Van Keulen and Röthlisberger (2017a) and the GTP charges as described by Meagher et al. (2003). The low-dielectric cavity ( $\epsilon_r = 4$ ) was described using Bondi atomic radii (1964) and the smoothed molecular surface definition of Brucolleri et al. (1997), while the solvent was modelled using a dielectric constant of 78, and a 150 mM concentration of salt with monovalent ions of radius  $1.5 \text{ \AA}$ . For the single species reactants, solution of the linearized PBE generated cubic potential grids with 129 grid points per dimension, spaced at  $1 \text{ \AA}$ , while larger grids with 161 points per dimension were generated for the binary reactants. Effective charges were calculated using the *ECM* module of SDA 7 (Gabdouline & Wade, 1996; Martinez et al, 2015),



with charge sites placed on the heteroatoms of ionized amino acid side chains and termini, the phosphate oxygen and phosphorus atoms of ATP and GTP, and  $Mg^{2+}$  ions. The effective charges of each solute were fitted such that, in a homogeneous dielectric environment, they reproduced the solute's electrostatic potential computed by solving the PBE in a skin bound by the surfaces described by rolling probe spheres of radii 4 and 7 Å along the molecular surface of the solute. Electrostatic desolvation potentials were calculated using the *make\_edhdlj\_grid* tool in SDA 7 (Martinez et al, 2015).

For each reaction, four BD simulations of 50 000 trajectories were performed using each MD snapshot, and rate constants were calculated using the Northrup, Allison and McCammon formalism (Northrup, Allison & McCammon, 1984). The mean and standard deviations across these four simulations was then determined. The average value for the corresponding rate constant was computed across all MD snapshots. The infinite dilution diffusion coefficients of each reaction species were calculated using HYDROPRO (García De La Torre, Huertas, & Carrasco, 2000; Ortega, Amorós, & García de la Torre, 2011) with the exception of those of the AC5 · G $\alpha$  complex reactants in the ternary complex forming reactions, for which the diffusion coefficients of AC5 were used. In each simulation trajectory, the position of the center of AC5, or the reactant complex, was fixed at the center of the simulated volume, while the initial position of the center of the reactant G $\alpha$  subunit was placed on the surface of a sphere of radius  $b$ , centered on the other reactant, with  $b$  taken as equal to the sum of the maximal extent of the distance of an atom of either reactant from the reactant center, plus the maximal extent of any interaction grid point to the solute center plus 30 Å. The simulations continued until the reactants diffused to a separation  $c$ , where  $c = 3b$ . Trajectories were assumed to have formed reactive encounter complexes when two independent native contacts between the two reactants reach a separation of 6.5 Å or less. Native contacts were defined as a pair of hydrogen bonding heteroatoms, separated by less than 5 Å in the bound complex. Two native contacts were assumed to be independent if the heteroatoms on the same solute that form the contacts were separated by more than 6 Å. This definition of an encounter complex has been shown to result in calculated protein-protein association rate constants that correlate well with experimental values (Gabdoulline and Wade, 2001).

## **Kinetic Model of the Signal Transduction Network**

The kinetic model of the signal transduction network is a system of coupled ordinary differential equations with mass-action kinetics

modeling the network's biochemical reactions. For example, for the reaction  $A+B \xrightleftharpoons[k_r]{k_f} C$ , the rate at which it occurs is given with:

$$v = \frac{d[C]}{dt} = - \frac{d[A]}{dt} = - \frac{d[B]}{dt} = k_f[A][B] - k_r[C]$$

In order to reduce the number of rate constants that would need estimation, our aim was to use a minimal model with which we could still study the coincidence detection ability of the enzyme and capitalize on the predictions of the molecular simulations. We have used two versions of the model, one with the allosteric exclusion and the other with the simultaneous binding scheme for AC5 regulation in Fig. 3. The full reaction networks are given in Fig. S14. The two versions of the model have 8 and 16 rate constants, respectively. In Fig. 3, we have additionally used versions of the model which included cAMP production to illustrate the correspondence between  $k_c$  and the levels of cAMP and thus rationalize the use of  $k_c$  as a proxy for the cAMP levels. The reactions and parameters for cAMP production and degradation have been taken from (Nair et al. 2019).

There are no receptors included in the model, and the  $Da \uparrow$  and  $ACh \downarrow$  inputs are modeled as changes in the rate constants for the conversion of inactive to active G proteins. Pools of inactive  $G_{\text{off}}$  and  $G_i$  are activated at rates of  $k_{fG_{\text{off}}} = 5 s^{-1}$  and  $k_{fG_i} = 5 s^{-1}$  when  $Da$  or  $ACh$  is present. This eliminates the parameters that would have corresponded to the reactions of ligand and receptor binding, and G protein and receptor binding. Additionally, we have omitted the heterotrimeric nature of the G proteins, i.e. we have not included the  $G\beta\gamma$  subunit in the model. The G proteins are modeled as simply switching between an active and inactive form. The value for the rate of  $G\alpha_i$  activation is chosen so that there is a high basal inhibition of AC5 by the tonic level of  $ACh$ , a reasonable assumption based on recent experimental results (Nair et al. 2019). The value for  $k_{fG_{\text{off}}}$  is, similarly, chosen to achieve amounts of active  $G_{\text{off}}$  high enough to drive the binding reactions with AC5 and  $AC5 \cdot G\alpha_i$  forward. The total amounts of AC5 and the two G proteins used for this model are  $n_{AC5} = 1500 \text{ nM}$ ,  $n_{G_{\text{off}}} = 1500 \text{ nM}$  and  $n_{G_i} = 6000 \text{ nM}$ .

The activated  $G\alpha_{\text{off}}$  and  $G\alpha_i$  interact with AC5 and can form each of the binary complexes and the ternary complex. Their deactivation is done by the intrinsic GTPase activity of the G proteins themselves, but is increased by AC5 for the case of  $G\alpha_s$  (a homologue to  $G\alpha_{\text{off}}$ ) at least

fivefold and the regulator of G protein signaling 9-2 (RGS9-2) for  $G\alpha_i$  20 to 40 times (Xie et al. 2012, Scholich et al. 1999), for which reason we have used values of  $k_{r_{G_{off}}}=0.5s^{-1}$  and  $k_{r_{G_i}}=5s^{-1}$ . If deactivated, the G proteins unbind from AC5. For the reverse (unbinding) rates of the G proteins from the binary AC5 complexes, we use values 100 times greater than the corresponding forward rate constants, which is the order of magnitude fitted in (Chen-Goodspeed et al., 2005). The reverse rates of G protein unbinding from the ternary complex, are increased by an order of magnitude compared to the reverse rates for unbinding from the respective binary complexes to qualitatively incorporate possible reduced stability of the ternary complex compared to the binary complexes on longer time scales indicated by the MD simulations.

The remaining parameters, the forward rate constants of the G proteins' binding to AC5 and the binary complexes  $AC5 \cdot G\alpha_{off}$  and  $AC5 \cdot G\alpha_i$ , were estimated with the BD simulations (see Table 1). We have also varied these to explore their effects on the network's ability to perform coincidence detection.

The kinetic model and related scripts to produce some of the figures can be found at <https://github.com/danieltrpevski/AC5-kinetic-model>.

## Measures of Coincidence Detection

As was defined in the introduction, for the signal transduction network that we consider, coincidence detection means to respond with significant amounts of cAMP only when the two incoming signals  $Da \uparrow$  and  $ACh \downarrow$  coincide in time and in the spatial vicinity of the receptors. Note that there are two aspects of coincidence detection in the definition:

- distinguishing between the inputs  $Da \uparrow + ACh \downarrow$ , and a  $Da \uparrow$  or  $ACh \downarrow$  alone, and
- responding strongly enough with amounts of cAMP that are physiologically relevant.

To quantify how well the network distinguishes between the different inputs, we use the synergy quantity, and to quantify the strength of the response, we use the average catalytic rate, both defined below.

**Average Catalytic Rate.** The average catalytic rate is an average of the catalytic rates of the unbound form of AC5 and each of the



complexes with the  $G\alpha$  subunits. For the allosteric exclusion scheme in Fig. 3B, where the ternary complex does not form, it is:

$$k_c = p_1 k_{c,AC5} + p_2 k_{c,AC5 \cdot G\alpha_{olf}} + p_3 k_{c,AC5 \cdot G\alpha_i}$$

with the weights

$$p_1 = \frac{[AC5]}{[AC5] + [AC5 \cdot G\alpha_{olf}] + [AC5 \cdot G\alpha_i]},$$

$$p_2 = \frac{[AC5 \cdot G\alpha_{olf}]}{[AC5] + [AC5 \cdot G\alpha_{olf}] + [AC5 \cdot G\alpha_i]},$$

$$p_3 = \frac{[AC5 \cdot G\alpha_i]}{[AC5] + [AC5 \cdot G\alpha_{olf}] + [AC5 \cdot G\alpha_i]}.$$

being the amounts of each enzyme species in the allosteric exclusion scheme as a fraction of the total concentration of AC5 in the system. For the simultaneous binding scheme where the ternary complex does form, the average catalytic rate is

$$k_c = q_1 k_{c,AC5} + q_2 k_{c,AC5 \cdot G\alpha_{olf}} + q_3 k_{c,AC5 \cdot G\alpha_i} + q_4 k_{c,G\alpha_{olf} \cdot AC5 \cdot G\alpha_i}$$

with

$$q_1 = \frac{[AC5]}{[AC5] + [AC5 \cdot G\alpha_{olf}] + [AC5 \cdot G\alpha_i] + [G\alpha_{olf} \cdot AC5 \cdot G\alpha_i]},$$

$$q_2 = \frac{[AC5 \cdot G\alpha_{olf}]}{[AC5] + [AC5 \cdot G\alpha_{olf}] + [AC5 \cdot G\alpha_i] + [G\alpha_{olf} \cdot AC5 \cdot G\alpha_i]},$$

$$q_3 = \frac{[AC5 \cdot G\alpha_i]}{[AC5] + [AC5 \cdot G\alpha_{olf}] + [AC5 \cdot G\alpha_i] + [G\alpha_{olf} \cdot AC5 \cdot G\alpha_i]},$$

$$q_4 = \frac{[G\alpha_{olf} \cdot AC5 \cdot G\alpha_i]}{[AC5] + [AC5 \cdot G\alpha_{olf}] + [AC5 \cdot G\alpha_i] + [G\alpha_{olf} \cdot AC5 \cdot G\alpha_i]}.$$

We assume that the catalytic rate of the unbound AC5 is  $k_{c,AC5}=0.1s^{-1}$ , and this rate is scaled by factors of  $\alpha_{G\alpha_{off}}$  and  $\alpha_{G\alpha_i}$  when the respective regulator G protein subunit binds:

$$k_{c,AC5 \cdot G\alpha_{off}} = \alpha_{G\alpha_{off}} k_{c,AC5}$$

$$k_{c,AC5 \cdot G\alpha_i} = \alpha_{G\alpha_i} k_{c,AC5}$$

The factors of stimulation and inhibition of AC5 are set to be  $\alpha_{G\alpha_{off}}=200$  and  $\alpha_{G\alpha_i}=0.01s^{-1}$  (Chen-Goodspeed et al. 2005). For the catalytic rate of the ternary complex, we use the result of the MD simulations that the ternary complex is inactive,  $\alpha_{G\alpha_{off},G\alpha_i}=\alpha_{G\alpha_i}$ , i.e.:

$$k_{c,G\alpha_{off} \cdot AC5 \cdot G\alpha_i} = \alpha_{G\alpha_i} k_{c,AC5},$$

except in Figs. 3D, 3E and 3F, where the catalytic rate of the ternary complex is varied to investigate its effect on coincidence detection.

**Synergy.** The synergy of two signals  $s_1$  and  $s_2$  is defined as

$$S(t) = \frac{r(s_1, s_2, t)}{r(s_1, t) + r(s_2, t) - r_{ss}},$$

where  $r_{ss}$  is the response at steady state. This quantity measures how strong the response  $r$  of the signal transduction network is for two coincident signals compared to the responses for single signals. The synergistic effect of the input signals can be examined in light of any quantity of interest in the network that is affected by the inputs, such as the level of activated PKA, for example (Nair et al. 2015). Not having included PKA or cAMP in the kinetic model, we use the average catalytic rate  $k_c$  as a proxy for the amount of cAMP produced, since the latter directly depends on  $k_c$ . That is, the synergy of a simultaneous Da  $\uparrow$  and ACh  $\downarrow$  is:

$$S(t) = \frac{k_c(Da \uparrow, ACh \downarrow, t)}{k_c(Da \uparrow, t) + k_c(ACh \downarrow, t) - k_{c,ss}}.$$

$S(t) > 1$  indicates a nonlinearly greater response in the presence of the two coincident signals,  $S(t) = 1$  indicates a linear response to the coincident signals, and  $S(t) < 1$  is a sublinear response. Hence, the case  $S(t) > 1$  indicates that the signal transduction network can perform coincidence detection, whereas  $S(t) \leq 1$  indicates an inability to do so.

Example traces for  $k_c$  and the corresponding synergy are given in Fig. 6. Using

$$\Delta = k_c(Da \uparrow, ACh \downarrow, t) - (k_c(Da \uparrow, t) + k_c(ACh \downarrow, t) - k_{c,ss})$$

to express the difference between the response of the network for two coincident signals and the response for single signals, the expression for the synergy can also be rewritten as

$$S(t) = \frac{k_c(Da \uparrow, ACh \downarrow, t)}{k_c(Da \uparrow, t) + k_c(ACh \downarrow, t) - k_{c,ss}} = 1 + \frac{\Delta}{k_c(Da \uparrow, t) + k_c(ACh \downarrow, t) - k_{c,ss}}.$$

The difference in the responses,  $\Delta$ , determines how big the synergistic effect of the input signals is (Fig. 6).

Figure 6 is an example depicting how  $k_c$  relates to the synergy. There are minimum and maximum bounds on  $k_c$ : it would attain the minimum value  $k_c^{\min}$  if all of AC5 were inhibited by  $G\alpha_i$ , that is, only the catalytically inactive complex  $AC5 \cdot G\alpha_i$  exists, where  $k_c^{\min}$  is the catalytic rate of  $AC5 \cdot G\alpha_i$  (see above). Analogously, it would attain the maximum value  $k_c^{\max}$  if all of AC5 were bound in the catalytically active complex  $AC5 \cdot G\alpha_{olf}$ , where  $k_c^{\max}$  is its catalytic rate (see above). In the models we use in this study, AC5 is never fully occupied by either of the  $G\alpha$  subunits, and hence  $k_c$  is always between the minimum and maximum bounds. To maximize  $\Delta$ , one would need to have  $k_c$  grow towards the maximum as much as possible during  $Da \uparrow + ACh \downarrow$ , and to have it as low as possible at steady state, and when each of the signals  $Da \uparrow$  and  $ACh \downarrow$  comes alone.

**The metric C combines S and  $k_c$ .** A combination of the average catalytic rate and the synergy gives a metric which can be helpful to evaluate whether the network both distinguishes between the different input situations and responds strongly. We use a product of  $k_c$  and S for this purpose,  $C = S k_c$ .

## Acknowledgements

This research has received funding from the European Union Seventh Framework Programme (FP7/2007-2013) under grant agreement N° 604102 (HBP) (JHK, PC, RCW), the European Union's Horizon 2020 Framework Programme for Research and Innovation under the Specific Grant Agreement N°s 720270 (Human Brain Project SGA1) (JHK, PC, RCW, UR, AGN) and 785907 (Human Brain Project SGA2) (JHK, PC, RCW, UR, DT), the Swedish e-Science Research Centre (SeRC) (JHK, DT), the Swedish Research Council (JHK, AGN, DT), the Klaus Tschira Stiftung (RCW, NJB), National Institute on Alcohol Abuse and Alcoholism Grant 2R01AA016022 (JHK). The authors thank Pietro Vidossich for scientific discussions during this project.

## Author contributions

PC, UR, RCW, and JHK conceived the study. AGN, NJB, DN, DT, SCvK, PC, RCW, UR and JHK designed the study. DN set up and performed the molecular dynamics simulations of ternary complexes and the *apo* AC5 · G $\alpha$ olf complex. SCvK prepared the starting structures of all MD simulations, set up and performed the MD simulation of the *apo* AC5 · G $\alpha$ i complex and helped setting up the simulations of the ternary complexes. DN and SCvK analyzed MD simulations. NJB performed and analyzed the Brownian dynamics simulations. DT performed the kinetic modeling and analyzed the results. SCvK and NJB performed the isoform sequence analysis. All authors analyzed the data. DT, DN, NJB and SCvK wrote the manuscript. AGN, RCW, PC, UR and JHK reviewed and revised the manuscript.

## Conflict of interest

The authors declare no conflicts of interest.

## References

Abraham MJ, Murtola T, Schulz R, Páll S, Smith JC, Hess B, Lindahl E. (2015). GROMACS: High performance molecular simulations through multi-level parallelism from laptops to supercomputers. *SoftwareX* 1, 19-25.

Allnér O, Nilsson L, & Villa A. (2012). Magnesium ion-water coordination and exchange in biomolecular simulations. *Journal of Chemical Theory and Computation.*, 8(4), 1493–1502.

Anholt RRH. (1994). Signal integration in the nervous system: adenylate cyclases as molecular coincidence detectors. *Trends in Neurosciences*, 17(1), 37–41. doi:10.1016/0166-2236(94)90033-7

Baker NA, Sept D, Joseph S, Holst MJ, & McCammon JA. (2001). Electrostatics of nanosystems: application to microtubules and the ribosome. *Proceedings of the National Academy of Sciences U. S. A.*, 98(18), 10037-10041. doi:10.1073/pnas.181342398

Bayer HM, and Glimcher PW. (2005) Midbrain Dopamine Neurons Encode a Quantitative Reward Prediction Error Signal. *Neuron* 47(1): 129-141, <https://doi.org/10.1016/j.neuron.2005.05.020>

Bekker H, Berendsen HJC, Dijkstra EJ, Achterop S, Van Drunen R, Van der Spoel D, Sijbers A, Keegstra H, and Renardus MKR. (1993). Gromacs: A parallel computer for molecular dynamics simulations. *Physics Computing*, 92:252–256.

Bondi A. (1964). van der Waals Volumes and Radii. *The Journal of Physical Chemistry*, 68(3), 441–451. doi:10.1021/j100785a001

Boras BW, Hirakis SP, Votapka LW, Malmstrom RD, Amaro RE, & McCulloch AD. (2015). Bridging scales through multiscale modeling: A case study on protein kinase A. *Frontiers in Physiology*, 6(SEP), 250. doi:/10.3389/fphys.2015.00250

Bourne, H. R., & Nicoll, R. (1993). Molecular machines integrate coincident synaptic signals. *Cell*, 72(1001), 65–75. doi:10.1016/S0092-8674(05)80029-7

Brand, C. S., Sadana, R., Malik, M., Smrcka, A. V., & Dessauer, C. W. (2015), Adenylyl Cyclase 5 Regulation by G Involves Isoform-Specific Use of Multiple Interaction Sites, *Molecular Pharmacology*, 88, 758-767.

Bruccoleri R, Novotny J, Davis M, & Sharp K. (1997). Finite difference Poisson-Boltzmann electrostatic calculations: Increased accuracy achieved by harmonic dielectric smoothing and charge antialiasing. *Journal of Computational Chemistry*, 18(2), 268-276. doi:10.1002/(SICI)1096-987X(19970130)18:2<268::AID-JCC11>3.0.CO;2-E

Changeux J-P. & Edelstein SJ. (2005). Allosteric mechanisms of Signal Transduction. *Science*, 308, 1424-1428.

Chen-Goodspeed M, Lukan AN, & Dessauer CW. (2005). Modeling of Gas and Gai regulation of human type V and VI adenylyl cyclase. *Journal of Biological Chemistry*, 280(3), 1808-1816. doi:10.1074/jbc.M409172200

Cooper DF. (2003) Regulation and organization of adenylyl cyclases and cAMP, *Biochem. J.* 375, 517-529. doi: 10.1042/BJ20031061

Cooper DF, and Crossthwaite AJ. (2006) Higher-order organization and regulation of adenylyl cyclases, *Trends in Pharmacological Sciences*, 27(8): 426-431. doi: <https://doi.org/10.1016/j.tips.2006.06.002>

Corvol JC, Studler JM, Schonn JS, Girault JA, & Hervé D. (2001). G $\alpha$ olf is necessary for coupling D1 and A2a receptors to adenylyl cyclase in the striatum. *Journal of Neurochemistry*, 76(5), 1585-1588. doi:10.1046/j.1471-4159.2001.00201.x

De Vries SJ, van Dijk M, & Bonvin AM. J. J. (2010). The haddock web server for data-driven biomolecular docking. *Nature Protocols*, 5(5):883-897, 4.

Delmeire D, Flamez D, Hinke SA, Cali JJ, Pipeleers D, & Schuit F. (2003). Type VIII adenylyl cyclase in rat beta cells: Coincidence signal detector/generator for glucose and GLP-1. *Diabetologia*, 46(10), 1383-1393. doi:10.1007/s00125-003-1203-8

Dessauer C. (2009) Adenylyl Cyclase-A-kinase Anchoring Protein Complexes: The Next Dimension in cAMP Signaling. *Molecular Pharmacology* 76 (5): 935-941

Dessauer CW, Tesmer JJG, Sprang SR, & Gilman AG. (1998). Identification of a Gi Binding Site on Type V Adenylyl Cyclase. *Journal of Biological Chemistry*, 273(40), 25831-25839. doi:10.1074/jbc.273.40.25831

Elcock,AH, Gabdoulline RR, Wade RC, & McCammon JA. (1999). Computer simulation of protein-protein association kinetics: acetylcholinesterase-fasciculin. *Journal of Molecular Biology*, 291(1), 149-162. doi:10.1006/jmbi.1999.2919

Eswar N, Webb B, Marti-Renom MA, Madhusudhan MS, Eramian D, Shen M, Pieper U, & Sali A. (2006). Comparative protein structure modeling using modeller. *Current Protocols in Bioinformatics*, 5-6.

Ferre S, Quiroz C, Woods AS, Cunha R, Popoli P, Ciruela F, Lluís C, Franco R, Azdad K, and Schiffmann SN. (2008) An Update on Adenosine A2A-Dopamine D2 Receptor Interactions: Implications for the Function of G Protein-Coupled Receptors. *Current Pharmaceutical Design*, 14, (15) 1468-1474(7)

Fino E, Glowinski J, & Venance L. (2005) Bidirectional Activity-Dependent Plasticity at Corticostriatal Synapses, *The Journal of Neuroscience* 25(49): 11279-11287

Fisher SD, Robertson PB, Black MJ, Redgrave P, Sagar MA, Abraham WC, and Reynolds JNJ (2017), Reinforcement determines the timing dependence of corticostriatal synaptic plasticity in vivo, *Nature Communications*, 8:334, doi: 10.1038/s41467-017-00394-x

Frezza E, Martin J, & Lavery R. (2018) A molecular dynamics study of adenylyl cyclase: The impact of ATP and G-protein binding. *PLoS ONE* 13(4): e0196207. <https://doi.org/10.1371/journal.pone.0196207>

Gabdoulline RR & Wade RC. (1996). Effective Charges for Macromolecules in Solvent. *Journal of Physical Chemistry*, 100(9), 3868-3878. doi:10.1021/jp953109f

Gabdoulline RR & Wade RC. (2001). Protein-protein association: investigation of factors influencing association rates by brownian dynamics simulations. *Journal of Molecular Biology*, 306(5), 1139-1155.

García De La Torre J, Huertas ML, & Carrasco B. (2000). Calculation of hydrodynamic properties of globular proteins from their atomic-level structure. *Biophysical Journal*, 78(2), 719-730. doi:10.1016/S0006-3495(00)76630-6

Glatt CE, & Snyder SH. (1993). Cloning and expression of an adenylyl cyclase localized to the corpus striatum. *Nature*, 361, 536-538. doi:10.1038/361536a0

Hahn DK, Tusell JR, Sprang SR & and Chu X. (2015) Catalytic Mechanism of Mammalian Adenylyl Cyclase: A Computational Investigation, *Biochemistry*, 54(40), 6252-6262. doi: 10.1021/acs.biochem.5b00655

Hervé D, Lévi-Strauss M, Marey-Semper I, Verney C, Tassin J-P, Glowinski J, & Girault J-A. (1993). Golf and Gs in Rat Basal Ganglia: Possible Involvement of Golf in the Coupling of Dopamine D1 Receptor with Adenylyl Cyclase. *Journal of Neuroscience*, 13(5), 2237-2248. doi:10.1523/JNEUROSCI.13-05-02237.1993

Hess BP. (2008). LINCS: A parallel linear constraint solver for molecular simulation. *Journal of Chemical Theory and Computation*. 4(1), 116-122. 7

Hollingsworth S, and Dror RO. (2018). Molecular Dynamics Simulation for All. *Neuron* 99(6): 1129-1143.

Hornak V, Abel R, Okur A, Strockbine B, Roitberg A & Simmerling C. (2006). Comparison of multiple Amber force fields and development of improved protein backbone parameters. *Proteins: Structure, Function, and Bioinformatics*. 65(3), 712-725.

Impey S, Wayman G, Wu Z, & Storm DR. (1994). Type I Adenylyl Cyclase Functions as a Coincidence Detector for Control of Cyclic AMP Response Element-Mediated Transcription: Synergistic Regulation of



Transcription by Ca<sup>2+</sup> and Isoproterenol. *Molecular and Cellular Biology*, 14(12), 8272–8281.

Jeon J, Dencker D, Wörtwein G, Woldbye DPD, Cui Y, Davis AA, Levey AI, Schütz G, Sager TN, Mørk A, Li C, Deng C-X, Fink-Jensen A and Wess J (2010). A Subpopulation of Neuronal M4 Muscarinic Acetylcholine Receptors Plays a Critical Role in Modulating Dopamine-Dependent Behaviors. *Journal of Neuroscience* 30 (6) 2396-2405, <https://doi.org/10.1523/JNEUROSCI.3843-09.2010>

Jorgensen WL, Chandrasekhar J, Madura JD, Impey RW & Klein ML. (1983). Comparison of simple potential functions for simulating liquid water. *The Journal of Chemical Physics*. 79(2), 926–935.

Joung IS & Cheatham III TE. (2008). Determination of alkali and halide monovalent ion parameters for use in explicitly solvated biomolecular simulations. *The Journal of Physical Chemistry B*. 112(30), 9020–9041.

Kitano H. (2002). Computational systems biology. *Nature*, 420(November), 206–210. doi:10.1142/S0219843613500102

Linder JU. (2006). Class III adenylyl cyclases: Molecular mechanisms of catalysis and regulation. *Cellular and Molecular Life Sciences*, 63(15), 1736–1751. doi:10.1007/s00018-006-6072-0

Linder JU, & Schultz JE. (2003). The class III adenylyl cyclases: Multi-purpose signalling modules. *Cellular Signalling*, 15(12), 1081–1089. doi:10.1016/S0898-6568(03)00130-X

Lui Y-H, Wenzel-Seifert K, & Seifert R. (2001). The olfactory G protein G $\alpha$ olf possesses a lower GDP-affinity and deactivates more rapidly than G $\alpha$ short: Consequences for receptor-coupling and adenylyl cyclase activation. *Journal of Neurochemistry*, 78(2), 325–338. doi:10.1046/j.1471-4159.2001.00422.x

Lustig KD, Conklin BR, Herzmark P, Taussig R, & Bourne HR. (1993). Type II adenylyl cyclase integrates coincident signals from G<sub>s</sub>, G<sub>i</sub>, and G<sub>q</sub>. *Journal of Biological Chemistry*, 268(19), 13900–13905.

Martí-Renom MA, Stuart AC, Fiser A, Sánchez R, Melo F & Sali A. (2000). Comparative protein structure modeling of genes and genomes. *Annual Review of Biophysics and Biomolecular Structure*, 29(1):291-325.

Martinez M, Bruce NJ, Romanowska J, Kokh DB, Ozboyaci M, Yu X, Öztürk MA, Richter S, & Wade RC. (2015). SDA 7: A modular and parallel implementation of the simulation of diffusional association software. *Journal of Computational Chemistry*, 36(21), 1631-1645. doi:10.1002/jcc.23971

McVey M, Hill J, Howlett A, & Klein C. (1999). Adenylyl cyclase, a coincidence detector for nitric oxide. *Journal of Biological Chemistry*, 274(27), 18887-18892. doi:10.1074/jbc.274.27.18887

Meagher KL, Redman LT, & Carlson HA. (2003). Development of polyphosphate parameters for use with the AMBER force field. *Journal of Computational Chemistry*, 24(9), 1016-1025. doi:10.1002/jcc.10262

Mons M, & Cooper DMF. (1994). Selective expression of one Ca<sup>2+</sup>-inhibitable adenylyl cyclase in dopaminergically innervated rat brain regions. *Molecular Brain Research*, 22, 236-244. doi:10.1016/0169-328X(94)90052-3

Mons N, Guillou JL, & Jaffard R. (1999). The role of Ca<sup>2+</sup>/calmodulin-stimulable adenylyl cyclases as molecular coincidence detectors in memory formation. *Cellular and Molecular Life Sciences*, 55(4), 525-533. doi:10.1007/s000180050311

Nair AG, Castro LRV, Khoury M. El, & Vincent P. (2019). The high efficacy of muscarinic M4 receptor in D1 medium spiny neurons reverses striatal hyperdopaminergia. *Neuropharmacology*, 146, 74-83. doi:10.1016/j.neuropharm.2018.11.029

Nair AG, Gutierrez-Arenas O, Eriksson O, Vincent P, & Hellgren Kotaleski J. (2015). Sensing Positive versus Negative Reward Signals through Adenylyl Cyclase-Coupled GPCRs in Direct and Indirect Pathway Striatal Medium Spiny Neurons. *Journal of Neuroscience*, 35(41), 14017-14030. doi:10.1523/JNEUROSCI.0730-15.2015

Nakamura T, Zhao Y, Yamagata Y, Hua YJ, and Yang W. (2012). Watching DNA polymerase  $\eta$  make a phosphodiester bond. *Nature*, 487(7406), 196-201. <https://doi.org/10.1038/nature11181>

Navarro G, Cordero, A, Casadó-Anguera, Moreno E, Cai N-S, Cortés A, Canela EI, Dessauer CW, Casadó V, Pardo L, Lluís C, and Ferré S. Evidence for functional pre-coupled complexes of receptor heteromers and adenylyl cyclase, *Nature Communications* 9, Article number: 1242 (2018), <https://doi.org/10.1038/s41467-018-03522-3>

Northrup SH, Allison SA, & McCammon JA. (1984). Brownian dynamics simulation of diffusion-influenced bimolecular reactions. *The Journal of Chemical Physics*, 80(4), 1517. doi:10.1063/1.446900

Onali P, Olanas MC. (2002) Muscarinic M4 receptor inhibition of dopamine D1-like receptor signalling in rat nucleus accumbens. *European Journal of Pharmacology* 448(2-3): 105-111, [https://doi.org/10.1016/S0014-2999\(02\)01910-6](https://doi.org/10.1016/S0014-2999(02)01910-6)

Ortega A, Amorós D, & García de la Torre J. (2011). Prediction of hydrodynamic and other solution properties of rigid proteins from atomic- and residue-level models. *Biophysical Journal*, 101(4), 892-898. doi:10.1016/j.bpj.2011.06.046

Pawlak V and Kerr JND. (2008) Dopamine Receptor Activation is Required for Corticostriatal Spike-Timing-Dependent Plasticity, *The Journal of Neuroscience* 28(10): 2435-2446

Sadana R, & Dessauer CW. (2009). Physiological roles for G protein-regulated adenylyl cyclase isoforms: insights from knockout and overexpression studies. *Neurosignals*, 17, 5-22. doi:10.1159/000166277

Scholich K, Mullenix JB, Wittpoth C, Poppleton HM, Pierre SC, Lindorfer MA, Garrison JC, Patel TB. (1999) Facilitation of signal onset and termination by adenylyl cyclase. *Science* 283:1328-1331, doi:10.1126/science.283.5406.1328

Schultz W. (2010) Dopamine signals for reward value and risk: basic and recent data. *Behavioral and Brain Functions* 6:24  
<https://doi.org/10.1186/1744-9081-6-24>

Seebacher T, Linder JU, & Schultz JE. (2001). An isoform-specific interaction of the membrane anchors affects mammalian adenylyl cyclase type V activity, *European Journal of Biochemistry*, 268, 105-110.

Shen W, Flajolet M, Greengard P, and Surmeier J. (2008) Dichotomous Dopaminergic control of striatal synaptic plasticity, *Science* 321(5890): 848-851

Stein M, Gabdouliline, RR, Wade RC. (2007). Bridging from molecular simulation to biochemical networks. *Current Opinion in Structural Biology*, 17(2), 166-72.

Steitz TA. (1993). DNA-and RNA-dependent DNA polymerases. *Current Opinion in Structural Biology*, 3(1), 31-38. [doi.org/10.1016/0959-440X\(93\)90198-T](https://doi.org/10.1016/0959-440X(93)90198-T)

Taussig R, Tang W-J, Hepler JR, and Gilman AG. (1994) Distinct Patterns of Bidirectional Regulation of Mammalian Adenylyl Cyclases, *The Journal of Biological Chemistry*, Vol. 269, No. 8, pp. 6093 -6100

Taussig R, Iniguez-Lluhi JA, & Gilman AG. (1992). Inhibition of Adenylyl Cyclase by G $\alpha$ . *Science*, 261, 218-221.

Tesmer JJG, Sunahara RK, Johnson RA, Gosselin G, Gilman AG, & Sprang SR. (1999). Two-metal-Ion catalysis in adenylyl cyclase. *Science*, 285(5428), 756-760. doi:10.1126/science.285.5428.756

Tesmer JJG and Sprang SR. (1998). The structure, catalytic mechanism and regulation of adenylyl cyclase. *Current opinion in structural biology*, 8(6), 713-719. [doi.org/10.1016/S0959-440X\(98\)80090-0](https://doi.org/10.1016/S0959-440X(98)80090-0)

Tesmer JJ, Sunahara RK, Gilman AG, & Sprang SR. (1997) Crystal structure of the catalytic domains of adenylyl cyclase in a complex with G $\alpha$ .GTP $\gamma$ S *Science* 278:1907-1916. doi:10.1126/science.278.5345.1907

Tong R, Wade RC, & Bruce NJ. (2016). Comparative electrostatic analysis of adenylyl cyclase for isoform dependent regulation properties. *Proteins: Structure, Function and Bioinformatics*, 84(13), 1844-1858. doi:10.1002/prot.25167

Van Keulen SC, & Rothlisberger U. (2017a). Effect of N-Terminal Myristoylation on the Active Conformation of G $\alpha$ i1-GTP. *Biochemistry*, 56(1), 271-280. doi:10.1021/acs.biochem.6b00388

Van Keulen SC, & Rothlisberger U. (2017b). Exploring the Inhibition Mechanism of Adenylyl Cyclase Type 5 by N-terminal Myristoylated G $\alpha$ i1:GTP. *PLoS Computational Biology*, 13(9), e1005673. doi:10.1371/journal.pcbi.1005673

Whisnant RE, Gilman AG, & Dessauer CW. (1996) Interaction of the two cytosolic domains of mammalian adenylyl cyclase. *Proceedings of the National Academy of Sciences of the United States of America* 93(13): p. 6621-6625. [doi.org/10.1073/pnas.93.13.6621](https://doi.org/10.1073/pnas.93.13.6621)

Xie K, Masuho I, Brand C, Dessauer CW, Martemyanov KA (2012) The complex of G protein regulator RGS9-2/G $\beta$ 5 controls sensitization and signaling kinetics of type 5 adenylyl cyclase. *Sci Signal* 5:ra63, doi:10.1126/scisignal.2002922, pmid:22932702.

Xie K, Masuho I, Shih C-C, Cao Y, Sasaki K, Lai CWJ, Han P-L, Ueda H, Dessauer CW, Ehrlich ME, Xu B, Willardson BM, Martemyanov KA. (2015) Stable G protein-effector complexes in striatal neurons: mechanism of assembly and role in neurotransmitter signaling, *eLife* 4: e10451. doi: 10.7554/eLife.10451

Yapo C, Nair AG, Clement L, Castro LR, Hellgren Kotaleski J, & Vincent P. (2017). Detection of phasic dopamine by D1 and D2 striatal medium spiny neurons. *Journal of Physiology*, 595(24), 7451-7475. doi:10.1113/JP274475

Zhang YF, and Cragg SJ. (2017) Pauses in Striatal Cholinergic Interneurons: What is Revealed by Their Common Themes and Variations? *Frontiers in Systems Neuroscience* 11:80. doi: 10.3389/fnsys.2017.00080

## Figure Legends

### Figure 1

A General scheme of the AC5 signal transduction network. It applies to both the D<sub>1</sub> and D<sub>2</sub> MSNs discussed in the text. Two agonists (L1 and L2) bind to two GPCRs (R1 and R2), releasing the G $\alpha_{olf}$  and G $\alpha_i$  subunits, respectively. These stimulate and inhibit the conversion of cAMP, respectively.

B Initial modelled configuration of the G $\alpha_{olf}$  · AC5 · G $\alpha_i$  ternary complex, used in the classical MD simulations. The cytosolic part of the AC5 enzyme consisting of the pseudo-symmetric C1 (blue) and C2 (red) cytoplasmic domains in an ATP-bound (green) conformation are complexed to an active conformation of G $\alpha_{olf}$  (gray) and to G $\alpha_i$  (cyan). GTP (orange) and the myristoyl moiety in G $\alpha_i$  (yellow) are shown in stick representation. Controlling the relative positions and conformations of C1 and C2 may enhance or inhibit enzymatic function. This is one way in which G $\alpha_{olf}$  and G $\alpha_i$  exert their regulatory effects: each of them has a separate binding site on the AC5 domain dimer.

### Figure 2 - Stability analysis of the *apo* ternary complex, conformation of the active site of AC5 in the *apo* state, and conformation of ATP in AC5's active site in the *holo* state.

A Initial conformation of the *apo* ternary complex including G $\alpha_{olf}$  (gray), G $\alpha_{i1}$  (cyan), C1 (blue), C2 (red). In addition to the protein structures, two GTP molecules as well as the myristoyl moiety of the G $\alpha_{i1}$  subunit and three Mg<sup>2+</sup> ions are shown. The green dashed line indicates the distance between the C $\alpha$  atom of Thr1007 (belonging to helix  $\alpha_4$ ) and the C $\alpha$  atom of Ser1208 (belonging to helix  $\alpha_4'$ ).

B RMSD of the backbone of the protein complexes G $\alpha_{olf}$  · AC5 · G $\alpha_{i1}$ , AC5 · G $\alpha_{olf}$  and AC5 · G $\alpha_{i1}$ .

C Time evolution of the distance between Thr1007 and Ser1208 for the three simulated complexes in *apo* form.

D Conformation of ATP in the G $\alpha_{olf}$  · AC5(ATP) · G $\alpha_{i1}$  system at different time intervals in the trajectory as well as the conformation of ATP $\alpha$ -S in



the AC · Gα<sub>s</sub> X-ray structure (PDB code 1CJK). The color of the time in green and orange corresponds to the coloured lines in image (E).

E Distance between the oxygen of a hydroxyl on the sugar ring of ATP, O3\*, and a Mg<sup>2+</sup> ion, (A) Mg<sup>2+</sup>, in the active site of the *holo* ternary complex. The black dashed line shows the distance between the two atoms in the AC · Gα<sub>s</sub> X-ray structure (PDB ID 1CJK) to which ATPα-S is bound (Tesmer 1999).

### **Figure 3 - The effect of the different regulatory schemes on coincidence detection.**

A The inputs to the model translate to an elevation in Gα<sub>of</sub> and pause in Gα<sub>i</sub>. The shaded parts of the scheme are not included in the kinetic model.

B The allosteric exclusion scheme, and the k<sub>c</sub>, synergy, and cAMP levels obtained due to this regulatory scheme.

C The simultaneous binding scheme, and the k<sub>c</sub>, synergy, and cAMP levels obtained due to this regulatory scheme.

D,E,F The effect of the ternary complex' catalytic activity on coincidence detection: the maximum of the synergy (D), the maximum of k<sub>c</sub> (E), the maximum of the metric C (F).

G The detection window for the allosteric occlusion scheme (red) and the simultaneous binding scheme (green). t<sub>Da</sub> ↑ and t<sub>ACh</sub> ↓ are the times when the Da ↑ and ACh ↓, respectively. Note the shared time axes in (A), (B) and (C).

### **Figure 4 - Dependence of coincidence detection on the forward rate constants.**

A, B, C The maximum of the synergy (A), the maximum of k<sub>c</sub> (B) and the maximum of the metric C (C) for a reduced rate constant k<sub>f4</sub> relative to the prediction from BD simulations.

D, E, F Coincidence detection for the simultaneous binding scheme as dependent on the forward rate constants: maximum of the synergy (D), maximum of k<sub>c</sub> (E), maximum of the metric C (F).

G, H, I Coincidence detection for the hindered simultaneous binding scheme as dependent on the forward rate constants: maximum of the synergy (G), maximum of  $k_c$  (H), maximum of the metric C (I). Axes are in units of  $(\text{nMs})^{-1}$ . Highlighted regions correspond to the forward rate constants predicted from BD simulations.

## Figure 5

A The structure of the C1 (blue and highlight colors) and C2 (red) catalytic domains of AC5.

B The highlighted regions show the AC5 residues that interact with  $G\alpha_i$  during complex formation. Overall sequence similarity for the C1 domain for the other mouse AC isoforms, compared to mouse AC5, and for the highlighted residues that interact with  $G\alpha_i$ .

C, D Pairwise sequence alignments for AC1 (C) and AC6 (D) with the colors matching those of the structure in subfigure A. The mouse sequences were taken from Uniprot, and aligned using Clustal Omega within Uniprot. The C1 domain was identified through alignment with PDB 1CJK (Tesmer et al., 1999), which contains a canine AC5 C1 domain, and the residues are numbered from the start of the C1 domain. The first residues of the C1 domains are at positions 288, 456 and 363 in the canonical sequences of AC1, AC5 and AC6 respectively. The red boxes in (C) indicate charge-altering substitutions between the AC5 and AC1 sequences in the  $G\alpha_i$  binding  $\alpha 3$  helix, while the blue box indicates a substitution in a residue whose mutation was found to affect  $G\alpha_i$ -induced inhibition of AC5 (Dessauer et al., 1998).

## Figure 6

A A cartoon of the average catalytic rate during each of the input situations  $Da \uparrow + ACh \downarrow$ ,  $Da \uparrow$ , and  $ACh \downarrow$ .

B The synergy corresponding to panel (A). In addition, the dashed and dotted lines illustrate how the synergy for a linear and a sublinear response would look like, respectively.

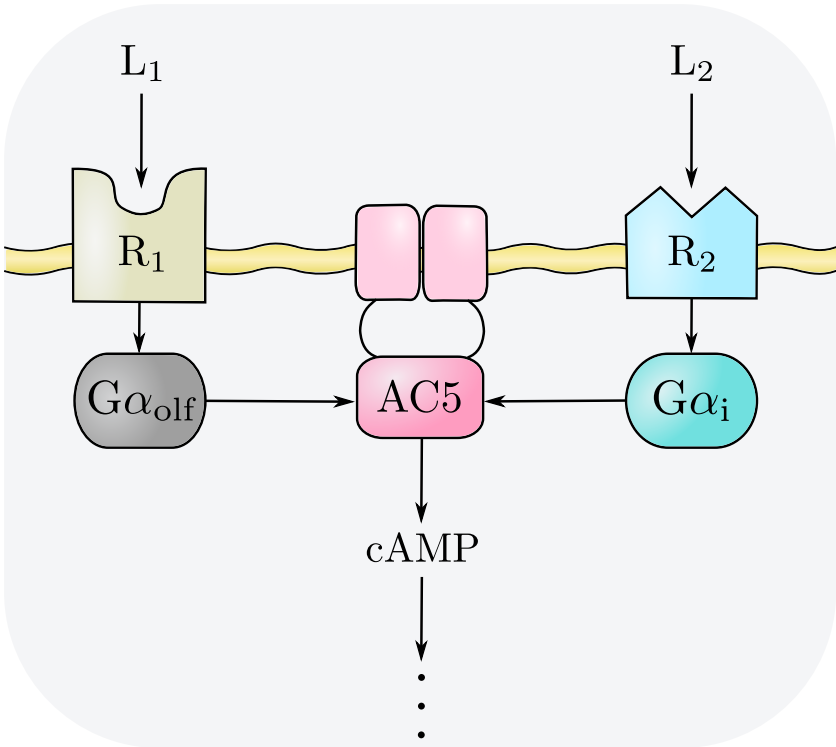
## Tables and their legends

**Table 1:** Bimolecular association rate constants ( $\text{nM}^{-1}\text{s}^{-1}$ ) for the forward reactions computed from BD simulations (standard deviation

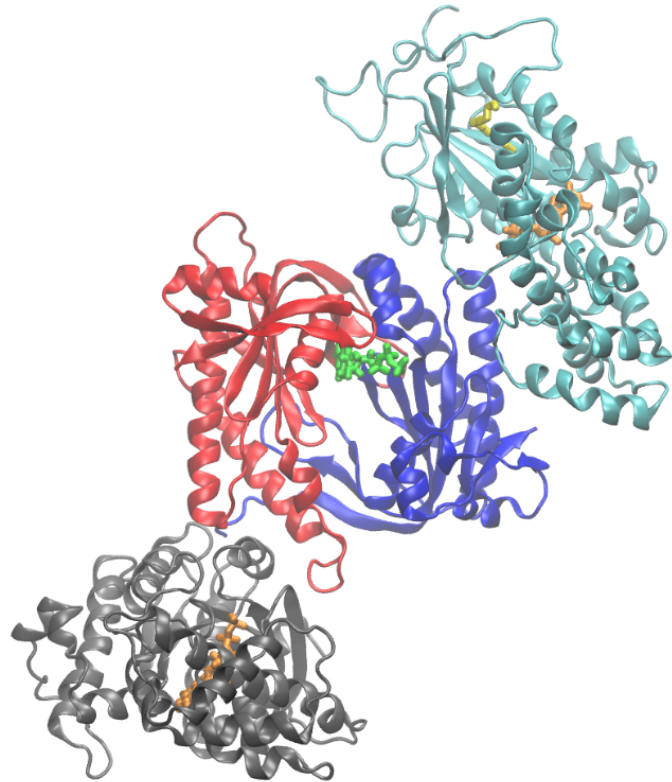
over all structures of complexes and replica simulations shown in parentheses). Rate constants were calculated separately for complexes incorporating both *apo* and *holo* AC5. Data for each individual structure of each complex are shown in Table S1.

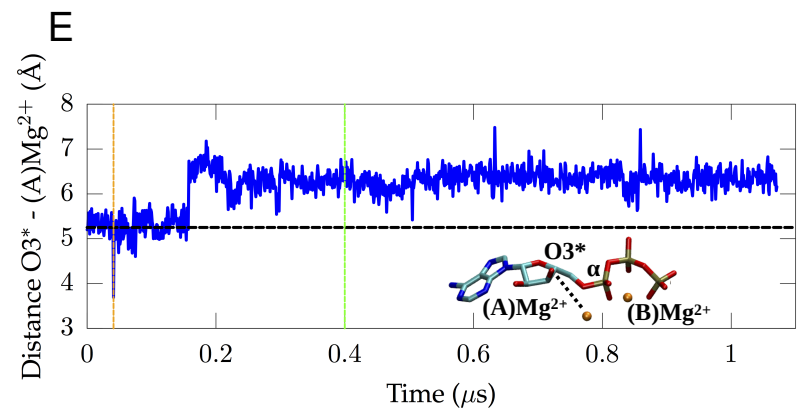
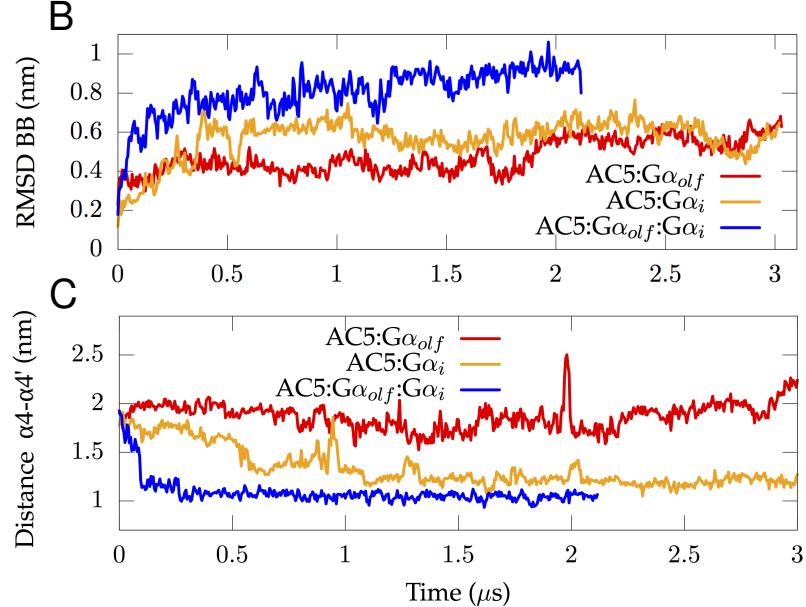
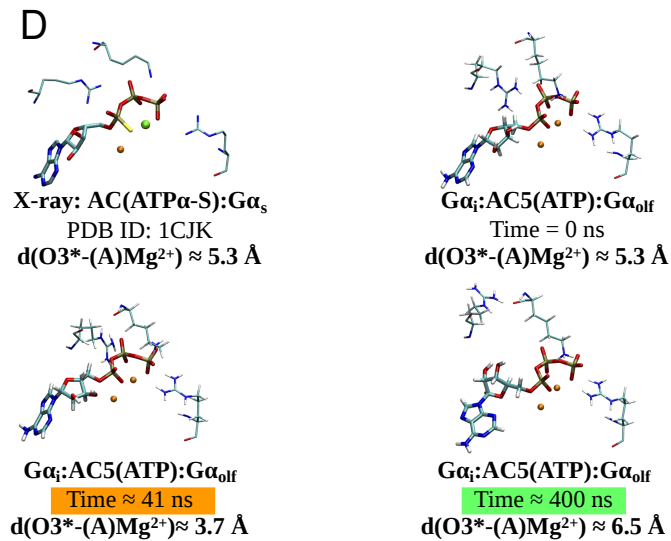
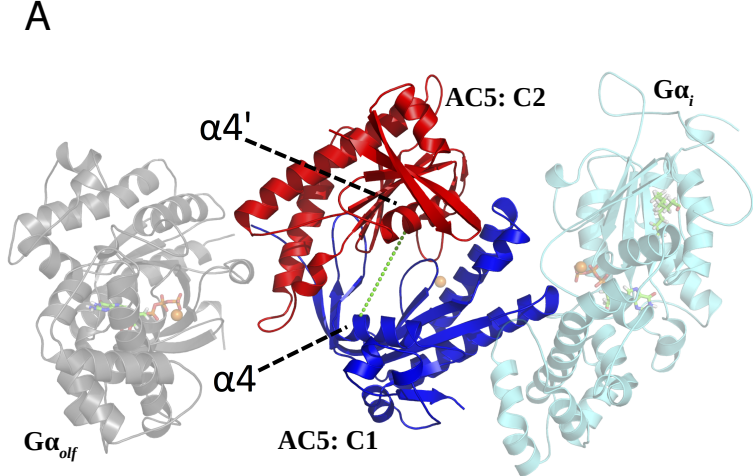
Rate Constant	<i>apo</i> AC5	<i>holo</i> AC5
$k_{f1}$	0.018 (0.007)	0.026 (0.009)
$k_{f2}$	0.02 (0.01)	0.05 (0.01)
$k_{f3}$	0.012 (0.008)	0.017 (0.006)
$k_{f4}$	0.02 (0.01)	0.020 (0.006)

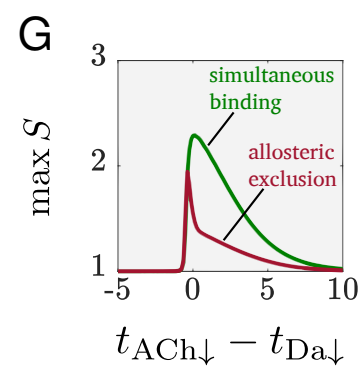
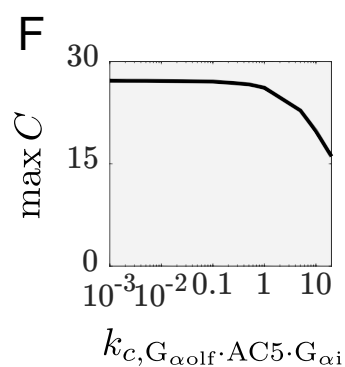
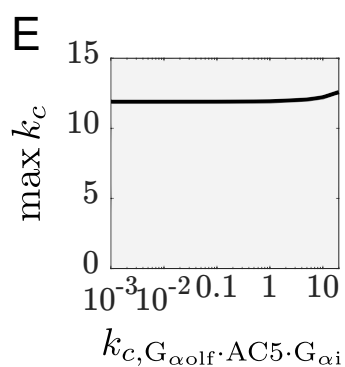
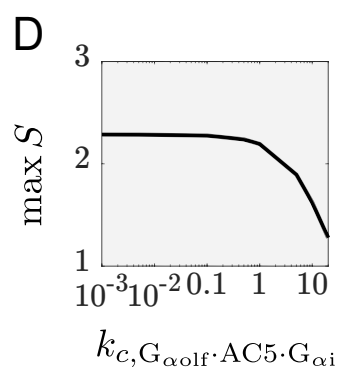
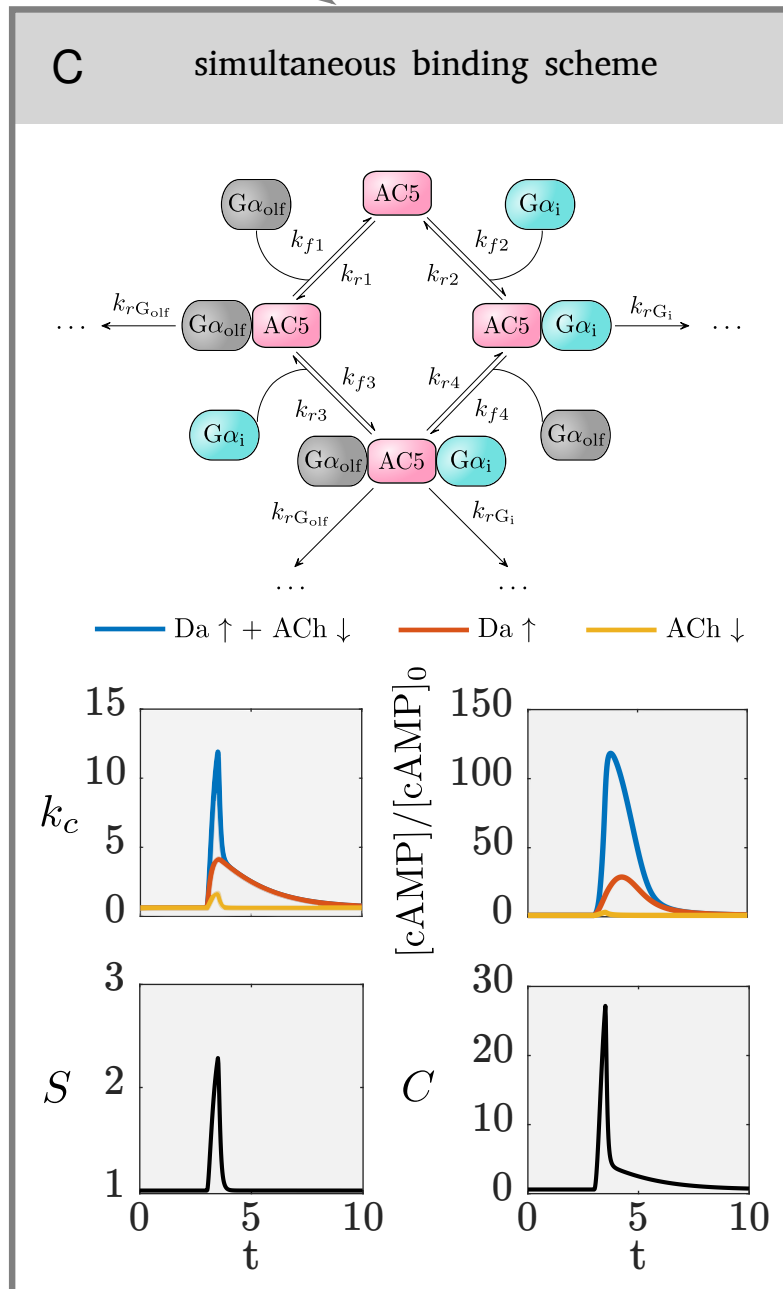
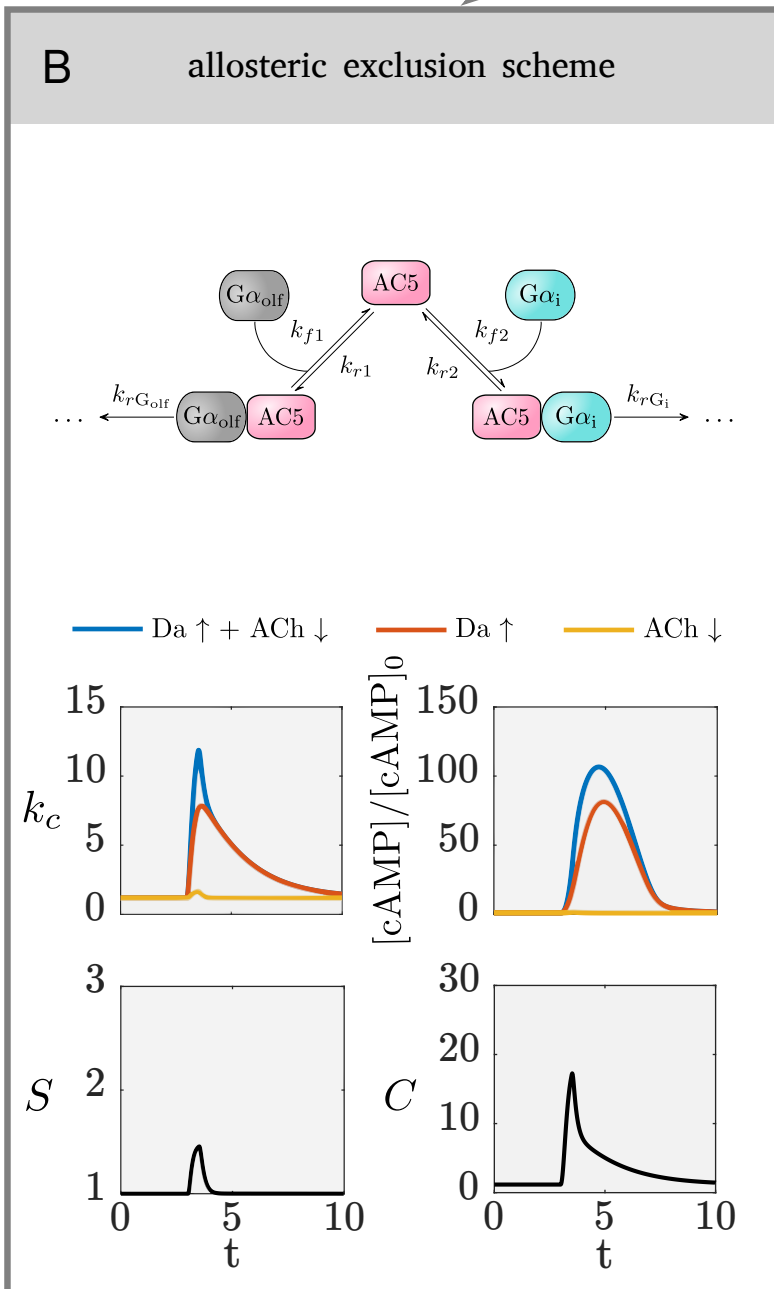
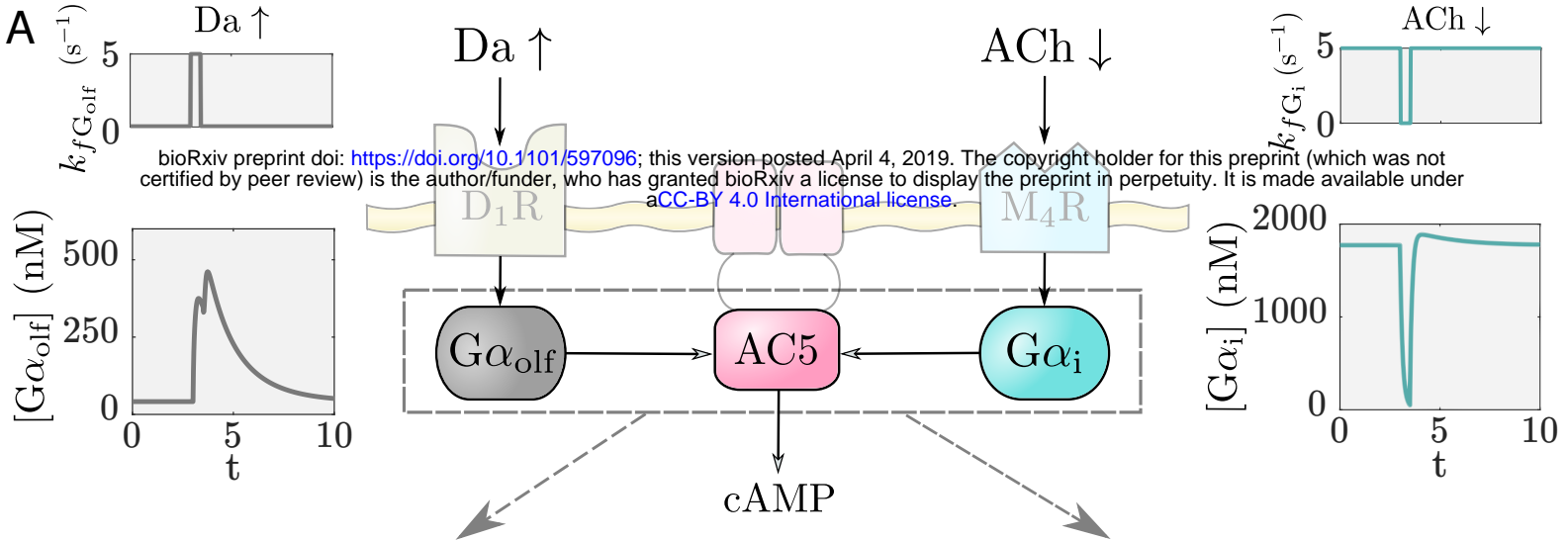
A



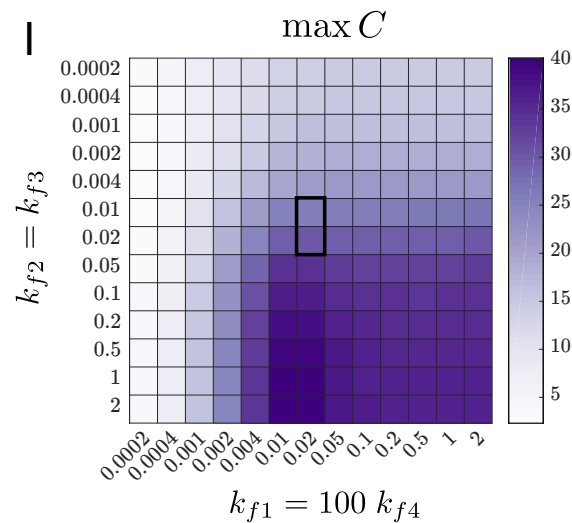
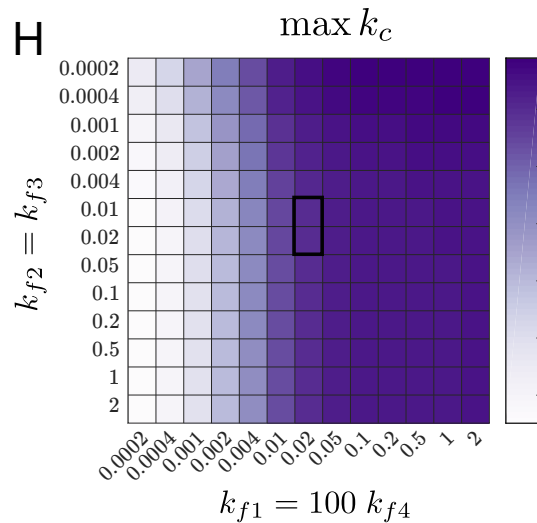
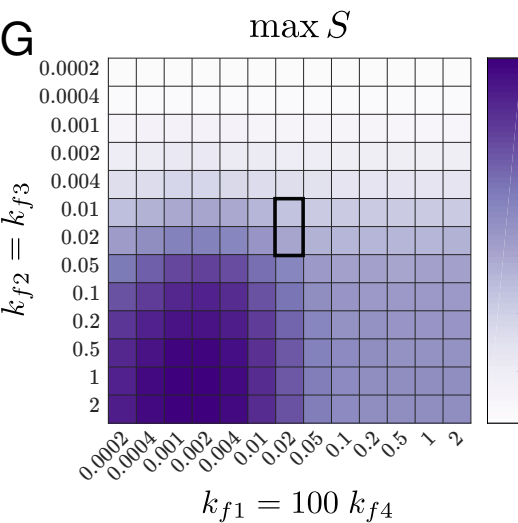
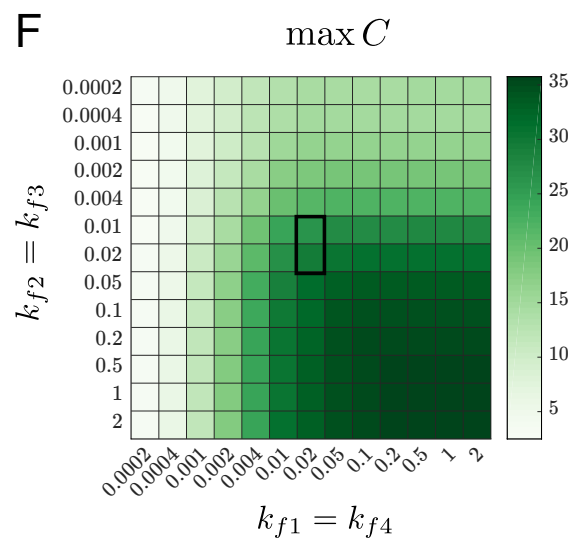
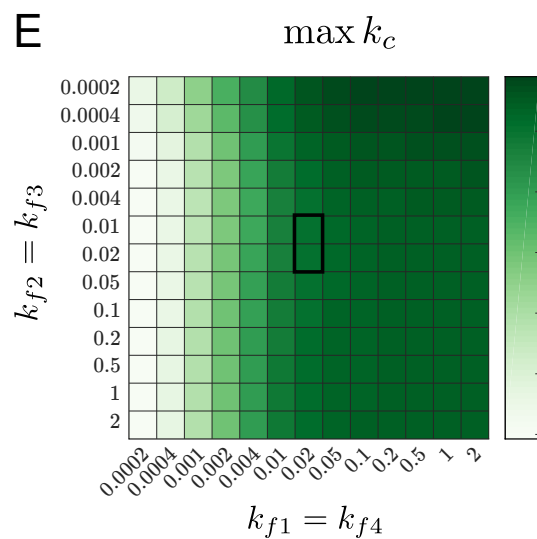
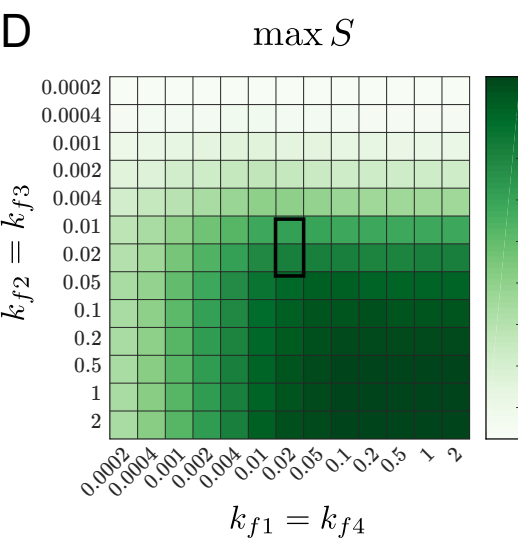
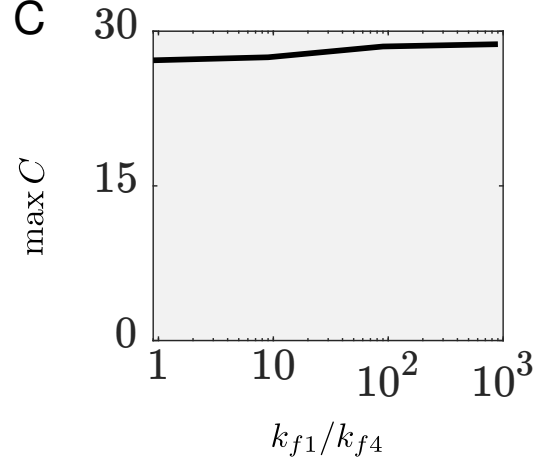
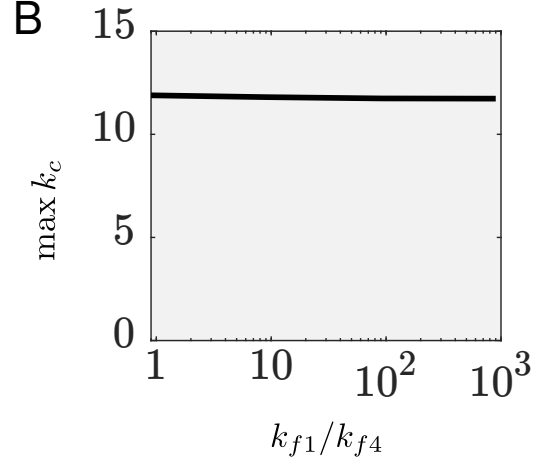
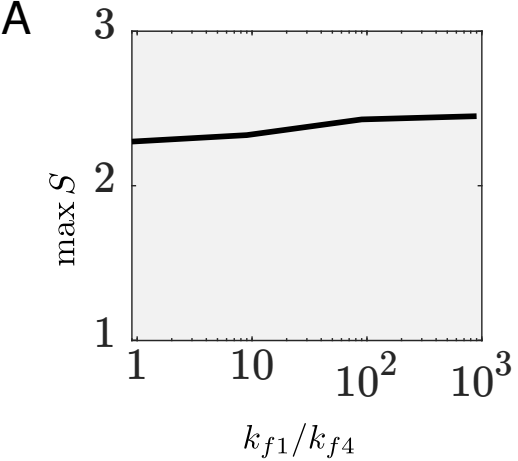
B



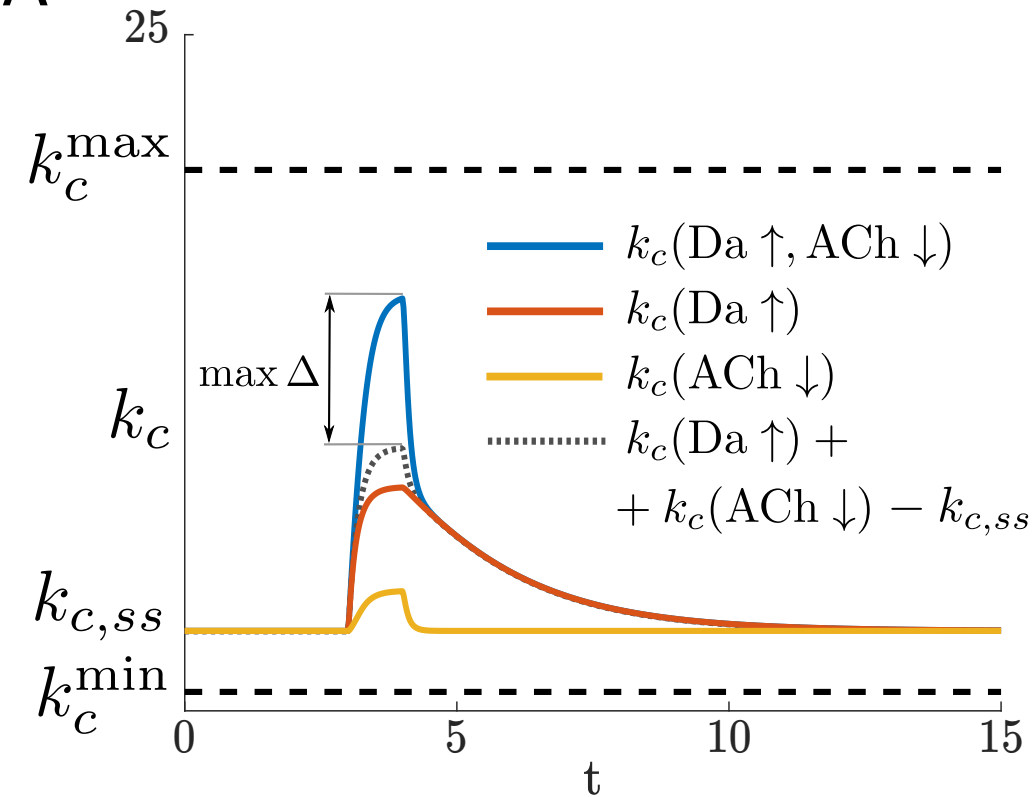
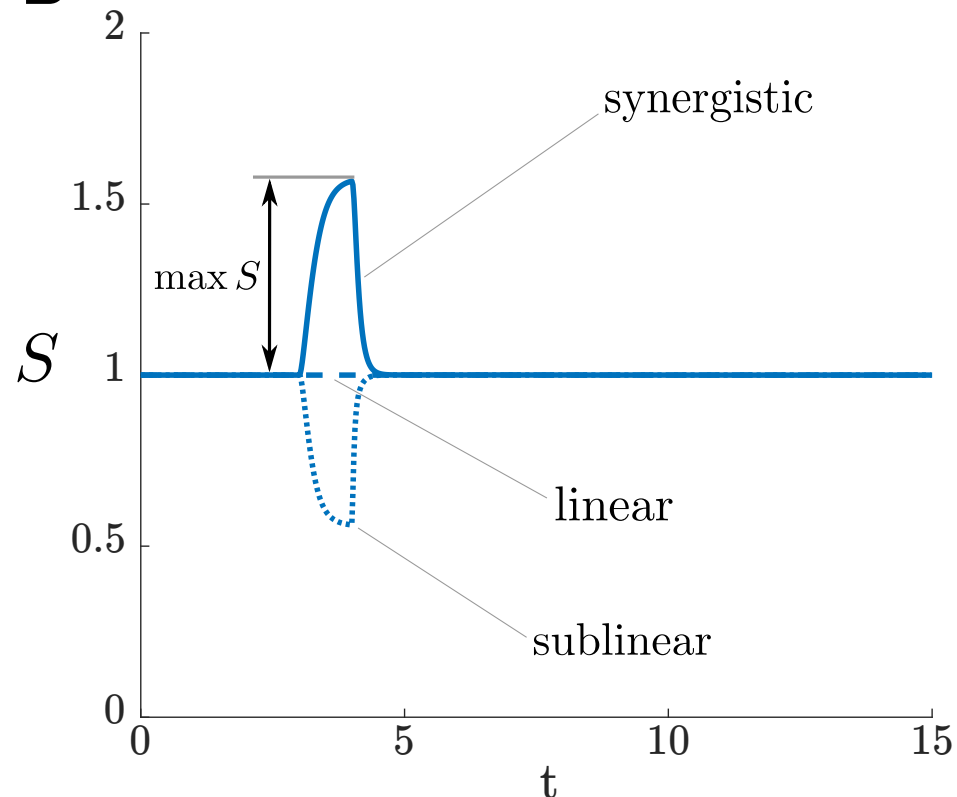










**A****B**

## Appendix

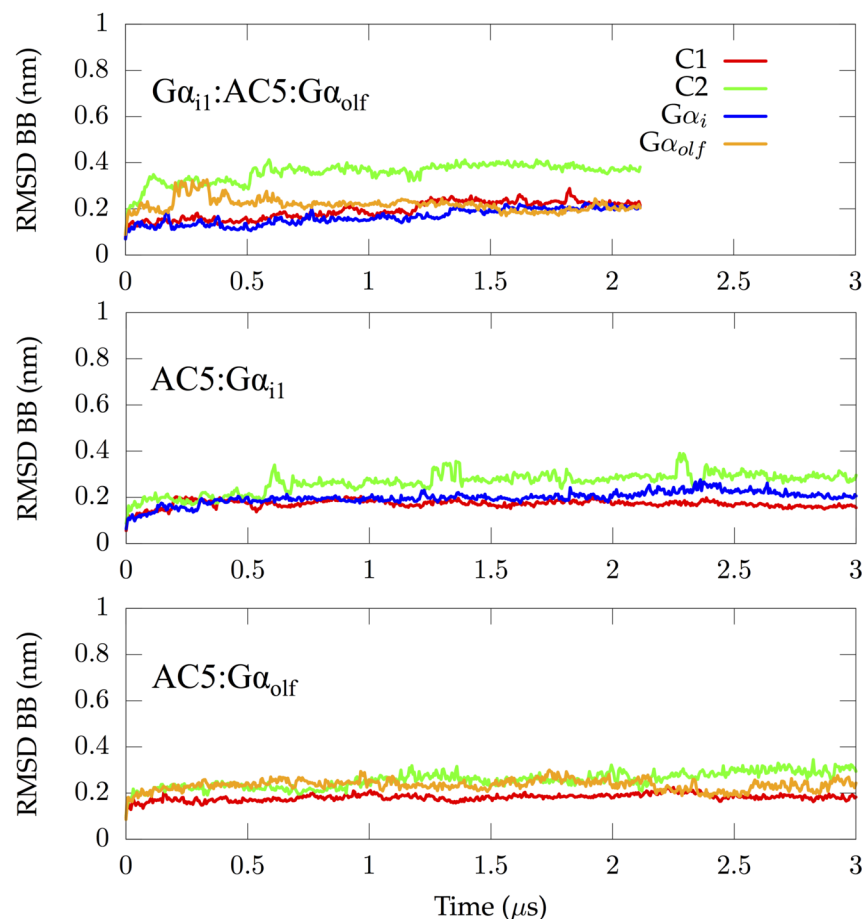


Figure S1: Root-mean-square deviations of three *apo* complexes:  $G\alpha_{olf} \cdot AC5 \cdot G\alpha_{i1}$ ,  $AC5 \cdot G\alpha_{i1}$  and  $AC5 \cdot G\alpha_{olf}$ . (Top panel) Individual RMSD values for C1, C2,  $G\alpha_{i1}$  and  $G\alpha_{olf}$  in the ternary complex only including the backbone of the domains. In the case of  $G\alpha_{i1}$ , residues 33 to 345 were taken into account during the RMSD calculation as the C and N termini are not structured. (Middle panel) Individual RMSD values for C1, C2 and  $G\alpha_{i1}$  in the binary  $AC5 \cdot G\alpha_{i1}$  complex only including the backbone of the domains. In the case of  $G\alpha_{i1}$ , residues 33 to 345 were taken into account during the RMSD calculation as the C and N termini are not structured. (Bottom panel) Individual RMSD values for C1, C2 and  $G\alpha_{olf}$  in the binary  $AC5 \cdot G\alpha_{olf}$  complex only including the backbone of the domains.

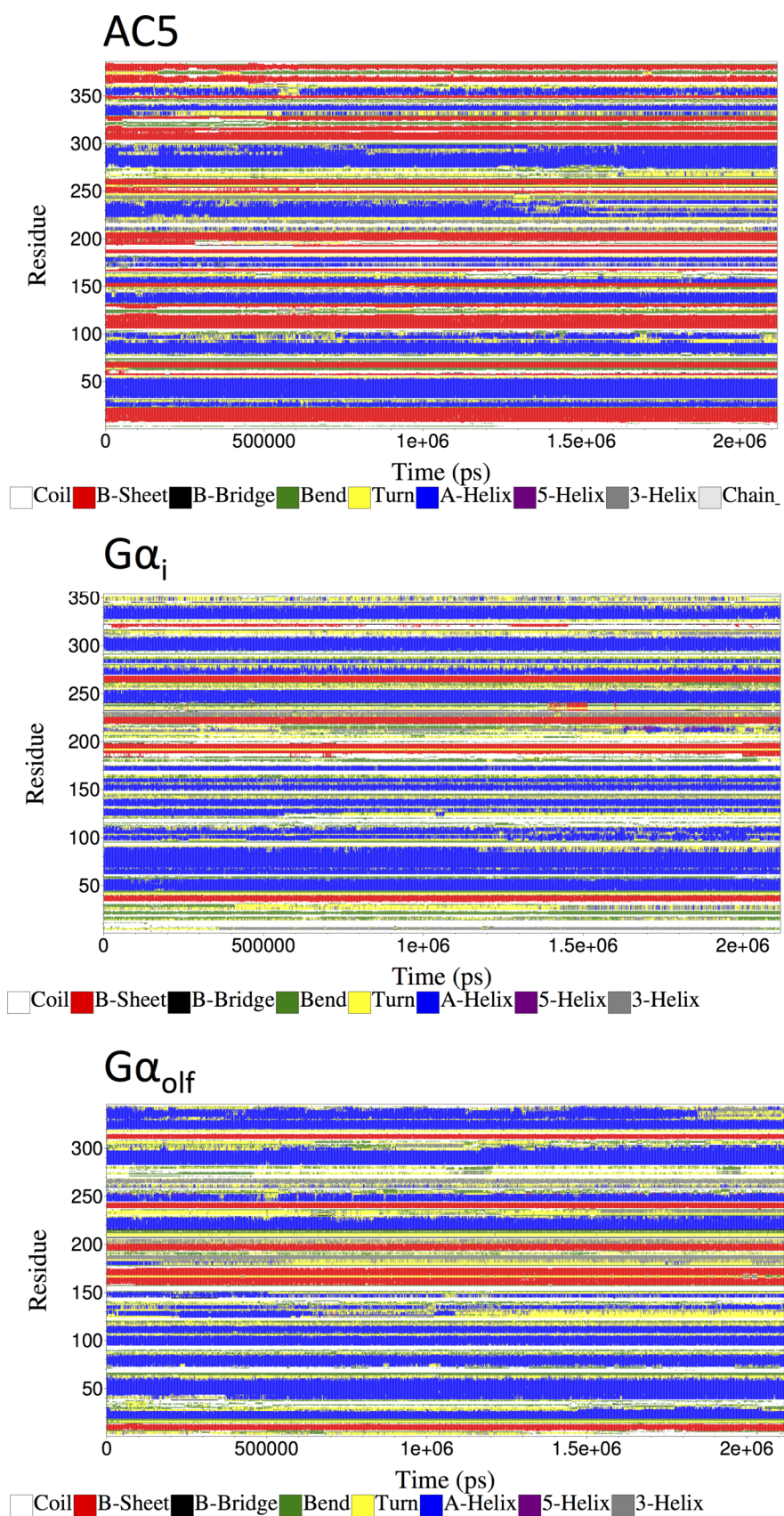


Figure S2: Time evolution of the secondary structures for AC5 (top),  $G\alpha_i$  (middle), and  $G\alpha_{olf}$  (bottom) along the trajectory of the *apo* ternary complex.



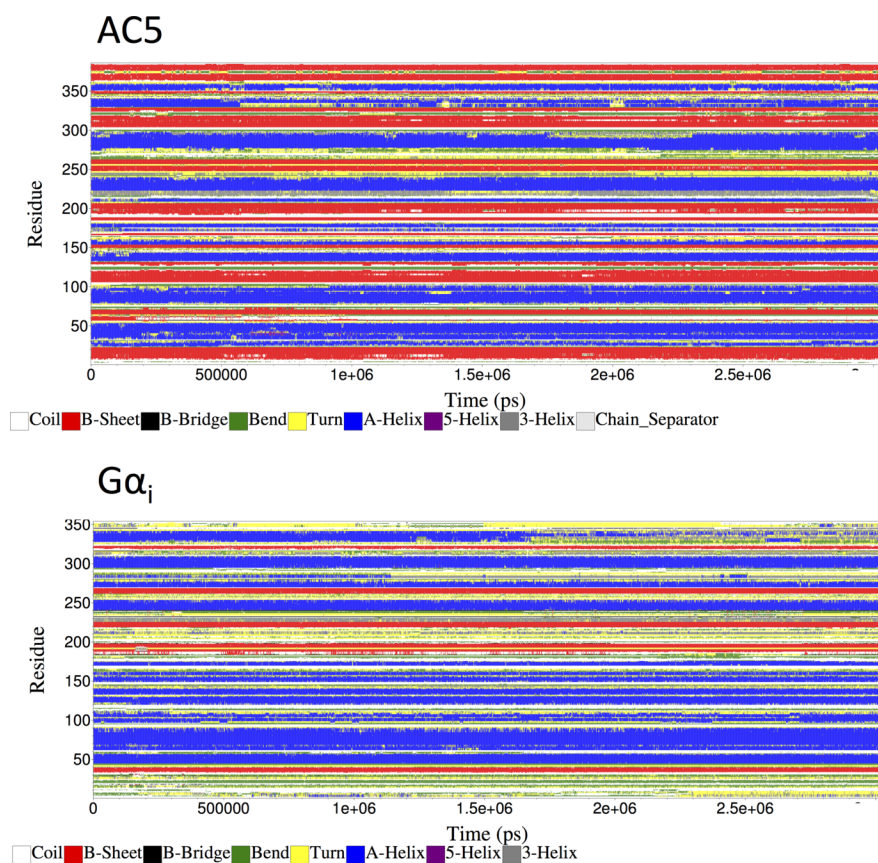


Figure S3: Time evolution of the secondary structures for AC5 (top), and G $\alpha_i$  (bottom), along the trajectory of the *apo* binary complex AC5 · G $\alpha_i$ .

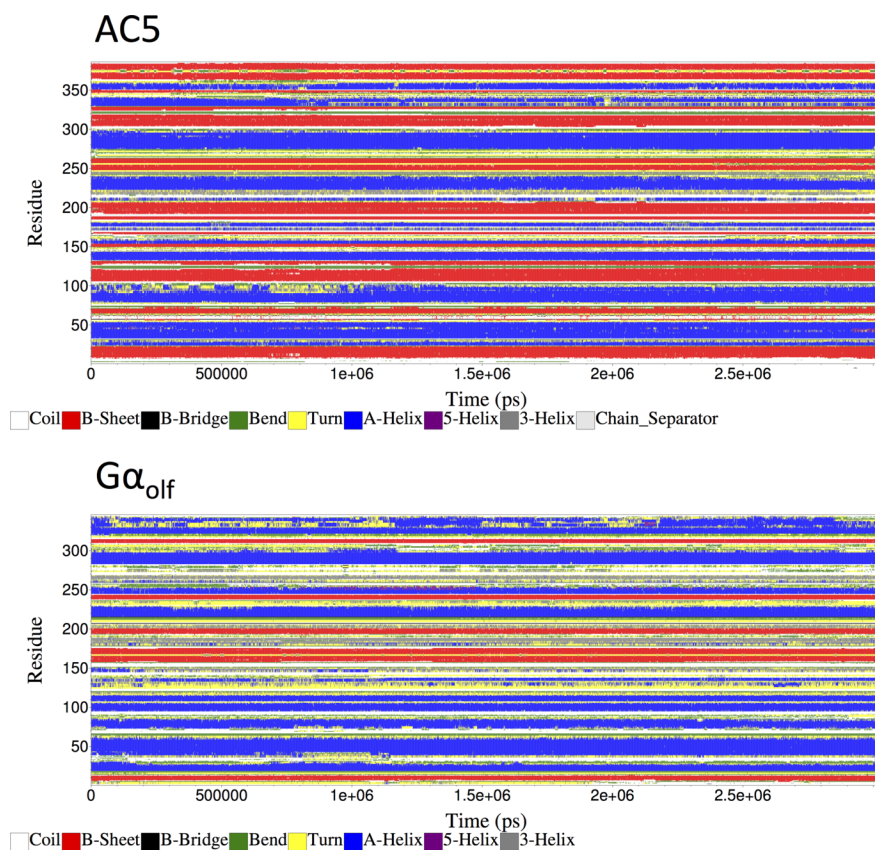


Figure S4: Time evolution of the secondary structures for AC5 (top), and  $G\alpha_{olf}$  (bottom), along the trajectory of the *apo* binary complex AC5 ·  $G\alpha_{olf}$ .

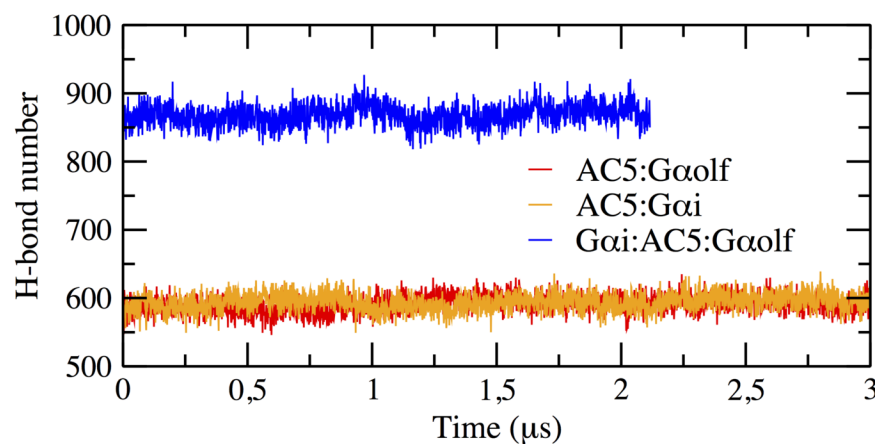


Figure S5: Time evolution of the number of hydrogen bonds present in the three simulated *apo* complexes along the respective MD trajectories.

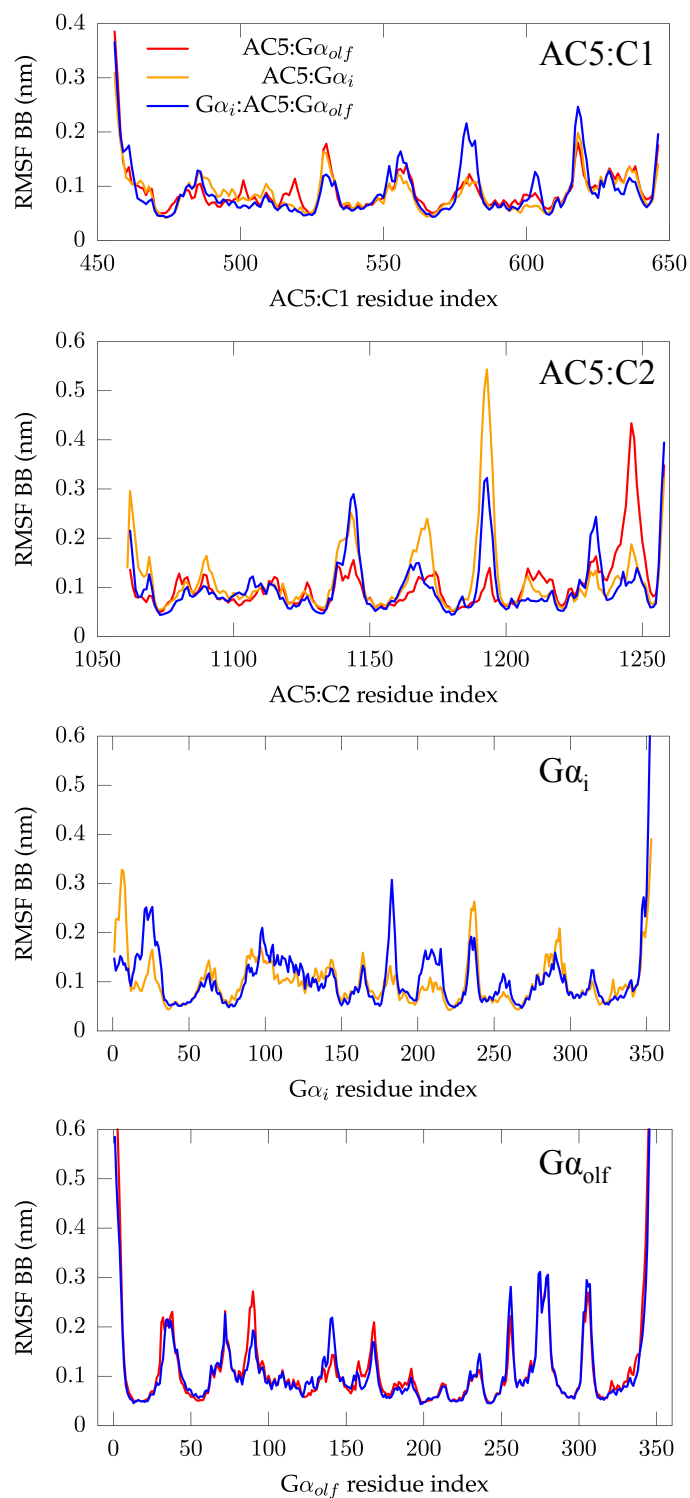


Figure S6: Root-mean-square fluctuations per residue calculated on the protein backbone of the different subunits (from top to bottom, AC5:C1, AC5:C2, G $\alpha_i$ , and G $\alpha_{olf}$ ) of the three simulated *apo* complexes.

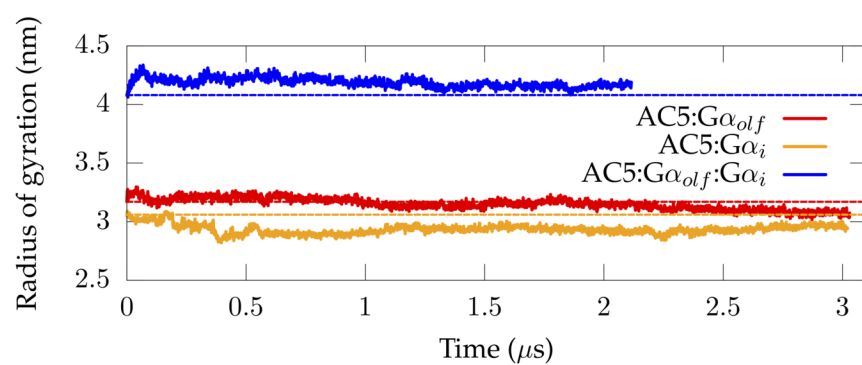


Figure S7: Radius of gyration calculated along the MD trajectories of the three simulated *apo* complexes,  $G_{\alpha_{olf}} \cdot AC5 \cdot G_{\alpha_i}$ ,  $AC5 \cdot G_{\alpha_i}$ , and  $AC5 \cdot G_{\alpha_{olf}}$ . The dashed lines indicate the values of the radius of gyration in the initial structures.

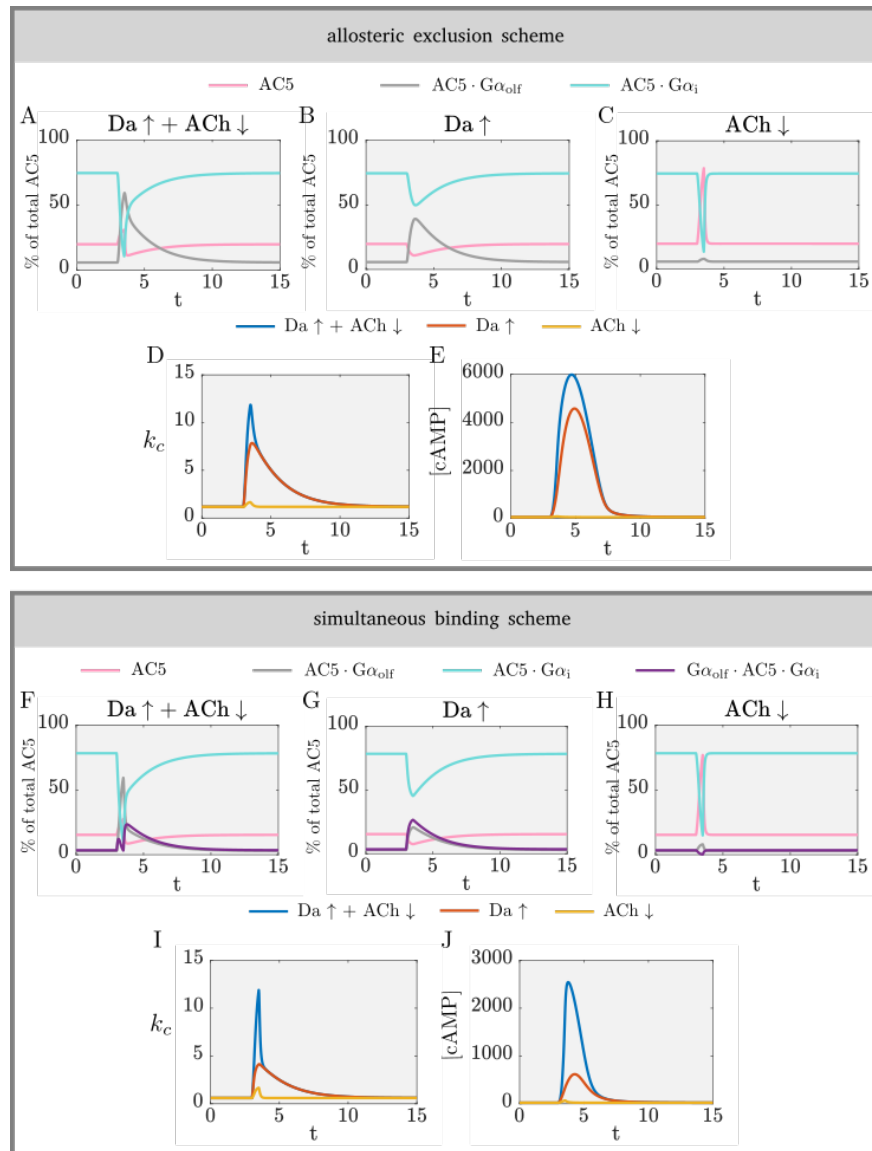


Figure S8: The effect of the interaction motif between AC5 and the regulatory G $\alpha$  subunits on coincidence detection. For the allosteric exclusion and simultaneous binding schemes, respectively, the amounts of each enzyme species as a percentage of the total amount of AC5 are shown for the cases of Da  $\uparrow$  + ACh  $\downarrow$  (A, F), Da  $\uparrow$  (B, G), and ACh  $\downarrow$  (C, H). (D, I) Average catalytic rate for each scheme. (E, J) cAMP levels for each scheme.

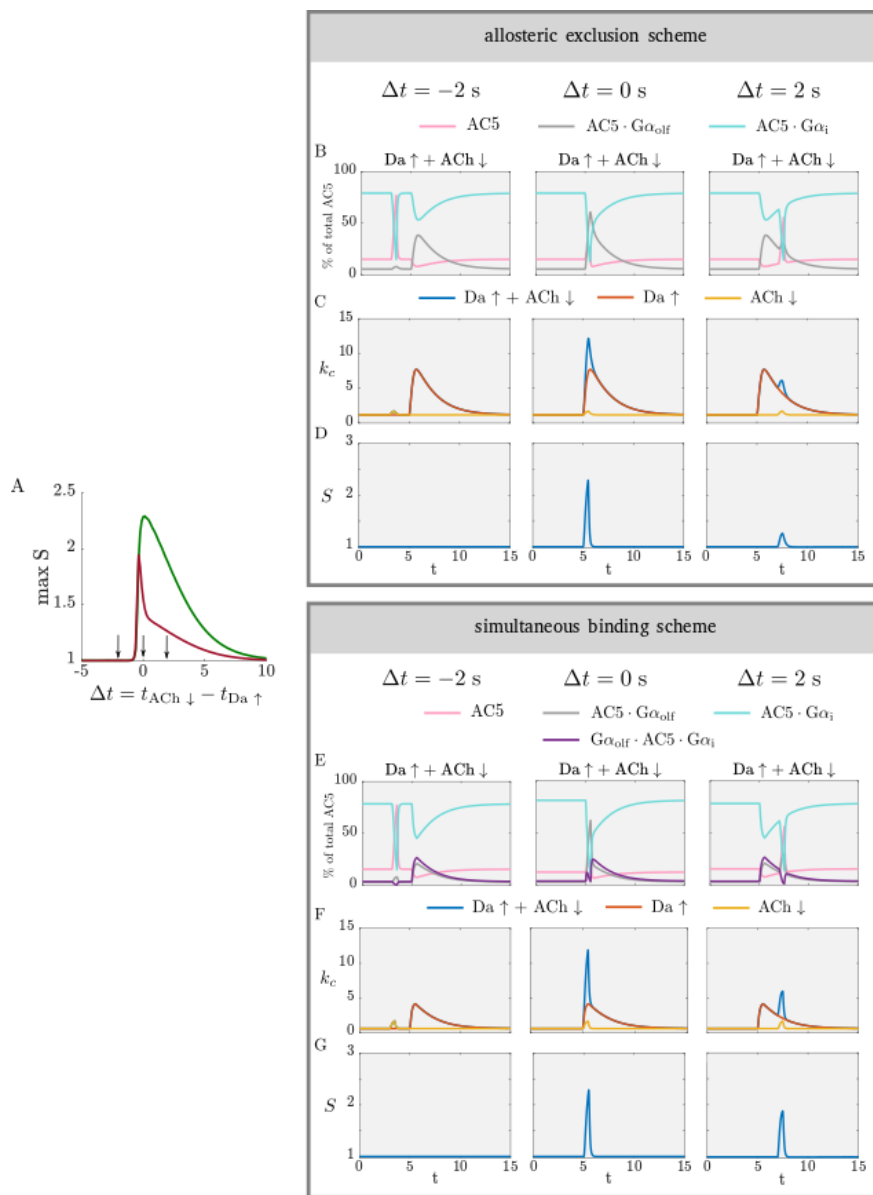


Figure S9: (A) The detection window for the allosteric exclusion scheme and simultaneous binding scheme. Arrows are the time differences between ACh  $\downarrow$  and Da  $\uparrow$  chosen for the traces below. (B) The percentage of each AC5 species as a fraction of the total amount of AC5, (C) average catalytic rate, (D) synergy for the allosteric exclusion scheme. (E), (F), and (G) are the same quantities for the simultaneous binding scheme. Note the shared axes.



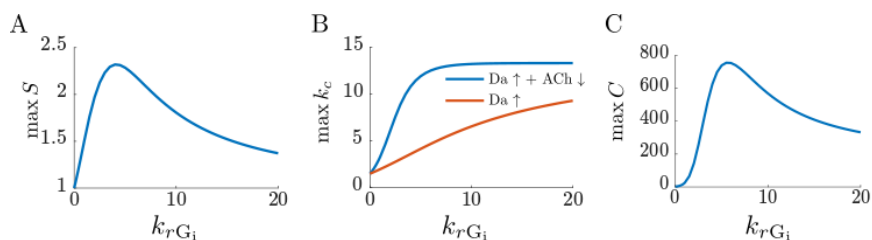


Figure S10: (A) The maximum of the synergy, (B) the maximum of  $k_c$ , (C) the maximum of the metric  $C$  as dependent on the rate of  $G\alpha_i$  deactivation,  $k_{rG_i}$ .

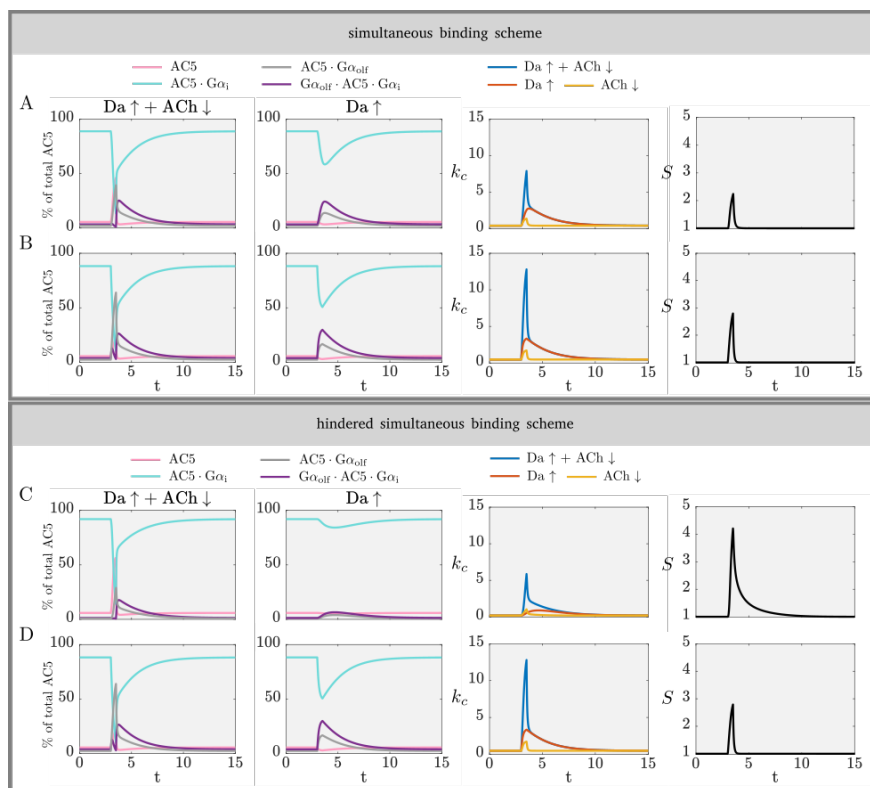


Figure S11: From left to right: the percentage of enzyme species for  $Da \uparrow + ACh \downarrow$ , the percentage of enzyme species for  $Da \uparrow$ , the average catalytic rate, and the synergy, for the simultaneous binding scheme for (A)  $k_{f1} = k_{f4} = 0.002 \text{ (nMs)}^{-1}$ ,  $k_{f2} = k_{f3} = 2 \text{ (nMs)}^{-1}$ , and (B)  $k_{f1} = k_{f4} = 2 \text{ (nMs)}^{-1}$ ,  $k_{f2} = k_{f3} = 2 \text{ (nMs)}^{-1}$  and the hindered simultaneous binding scheme for (C)  $k_{f1} = 0.002 \text{ (nMs)}^{-1}$ ,  $k_{f2} = k_{f3} = 2 \text{ (nMs)}^{-1}$  and (D)  $k_{f1} = 2 \text{ (nMs)}^{-1}$ ,  $k_{f2} = k_{f3} = 2 \text{ (nMs)}^{-1}$ . Note the shared axes.

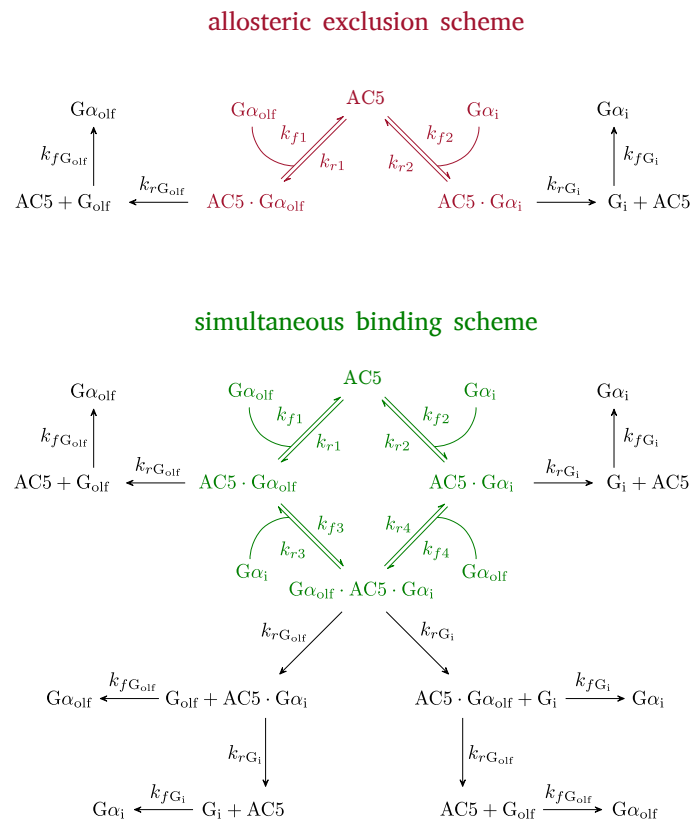


Figure S12: The full kinetic models of the signal transduction networks used in this study.





**Table S1.** Bimolecular association rate constants (nMs)<sup>-1</sup> for the forward reactions computed via BD simulations. Each rate constant was calculated using a number of snapshots from MD simulations. The reported numbers for each snapshot are the mean values estimated from 4 BD simulations of 50 000 trajectories (standard deviation in parentheses). Rate constants were calculated for complexes including *apo* and *holo* AC5 (superscripts a and h respectively).

MD snapshot	$k_{f1}^a$	$k_{f1}^h$	$k_{f2}^a$	$k_{f2}^h$
1	0.003 (0.002)	0.013 (0.004)	0.015 (0.002)	0.005 (0.002)
2	0.011 (0.003)	0.045 (0.007)	0.018 (0.006)	0.028 (0.004)
3	0.038 (0.003)	0.019 (0.002)	0.036 (0.006)	0.10 (0.01)
4	0.022 (0.006)		0.008 (0.003)	0.061 (0.006)
5			0.016 (0.003)	
6			0.013 (0.003)	
7			0.027 (0.005)	
Mean	0.018 (0.007)	0.026 (0.009)	0.02 (0.01)	0.05 (0.01)

MD snapshot	$k_{f3}^a$	$k_{f3}^h$	$k_{f4}^a$	$k_{f4}^h$
1	0.009 (0.003)	0.004 (0.001)	0.037 (0.004)	0.035 (0.004)
2	0.004 (0.001)	0.017 (0.004)	0.007 (0.003)	0.016 (0.003)
3	0.011 (0.005)	0.032 (0.004)	0.007 (0.003)	0.013 (0.002)
4	0.005 (0.002)	0.016 (0.002)	0.0087 (0.0007)	0.016 (0.003)
5	0.030 (0.004)		0.06 (0.01)	
6				
7				
Mean	0.012 (0.008)	0.017 (0.006)	0.02 (0.01)	0.020 (0.006)

## The allosteric exclusion scheme inherently lacks the ability for coincidence detection

To show this we make the following simplifications:

1. During a Da  $\uparrow$  and a ACh  $\downarrow$ , respectively, the rise in  $[G\alpha_{olf}]$  and drop in  $[G\alpha_i]$  are square-shaped, i.e. the interactions between the G proteins and AC5 are fast so that the transient steady state levels in the network are achieved quickly and last for the whole duration of the signals

2. During the  $Da \uparrow$ , enough  $G\alpha_{olf}$  is produced to occupy all AC5, i.e.  $[G\alpha_{olf}] \gg [G\alpha_i]$  and  $[G\alpha_{olf}]$  is at a saturating level.
3. During the  $ACh \downarrow$ ,  $[G\alpha_i]$  drops to approximately 0, i.e. all available AC5 is disinhibited from  $G\alpha_i$ ;

We consider what happens in the limiting cases of ‘perfect’ stimulation and inhibition of AC5, i.e.  $\alpha_{G_{olf}} \rightarrow \infty$  and  $\alpha_{G_i} = 0$ . With these assumptions only the effect of the structure of the regulatory scheme on coincidence detection is isolated.

We now determine the synergy of this scheme. The expression for the synergy is repeated here for convenience:

$$S(t) = \frac{k_c(Da\uparrow, ACh\downarrow, t)}{k_c(Da\uparrow, t) + k_c(ACh\downarrow, t) - k_{c,ss}}$$

Each of the terms in the expression for the synergy are as follows. For a  $Da \uparrow + ACh \downarrow$ , there is no  $G\alpha_i$  in the system during a  $ACh \downarrow$ , so all AC5 is occupied by the produced saturating concentration of  $G\alpha_{olf}$ .

$$k_c(Da \uparrow + ACh \downarrow, t) = k_{c, AC5 \cdot G\alpha_{olf}} = \alpha_{G_{olf}} k_{c, AC5}$$

For only a  $Da \uparrow$ , there is enough  $G\alpha_{olf}$  to outcompete  $G\alpha_i$  in the occupation of AC5, and AC5 is saturated with  $G\alpha_{olf}$ , which yields the same result as for  $k_c(Da \uparrow + ACh \downarrow)$ :

$$k_c(Da \uparrow, t) = k_{c, AC5 \cdot G\alpha_{olf}} = \alpha_{G_{olf}} k_{c, AC5}$$

For only an  $ACh \downarrow$ , there is no  $G\alpha_i$  in the system and AC5 is partly occupied by any basal levels of  $G\alpha_{olf}$ :

$$k_c(ACh \downarrow, t) = p_4 k_{c, AC5} + p_5 k_{c, AC5 \cdot G\alpha_{olf}},$$

where

$$p_4 = \frac{[AC5 \cdot G\alpha_{olf}]_{ACh\downarrow}}{[AC5]_{ACh\downarrow} + [AC5 \cdot G\alpha_{olf}]_{ACh\downarrow}}, \text{ and}$$

$$p_5 = \frac{[AC5 \cdot G\alpha_i]_{ACh\downarrow}}{[AC5]_{ACh\downarrow} + [AC5 \cdot G\alpha_i]_{ACh\downarrow}} = 1 - p_4.$$

The steady state value for  $k_c$  is given under the section ‘Average catalytic rate’ in the Methods of the main text. Substituting these expressions in the expression for the synergy, and taking the limit  $\alpha_{G_{olf}} \rightarrow \infty$  yields:

$$S_{\alpha_{G_{olf}} \rightarrow \infty} \rightarrow \frac{1 - p_2}{1 - p_2 + p_5 - p_2} < 1.$$

The synergy is always less than 1 since  $p_5 > p_2$ , i.e.  $p_5$  is the proportion of  $AC5 \cdot G\alpha_{olf}$  when there is no  $G\alpha_i$  in the system, which is always greater than  $p_2$ , the proportion of  $AC5 \cdot G\alpha_{olf}$



bioRxiv preprint doi: <https://doi.org/10.1101/597096>; this version posted April 4, 2019. The copyright holder for this preprint (which was not certified by peer review) is the author/funder, who has granted bioRxiv a license to display the preprint in perpetuity. It is made available under aCC-BY 4.0 International license.

when there is no  $G\alpha_i$  in the basal state, when there is  $G_i$  in the system.